arXiv:hep-ex/0603022 v1   10 Mar 2006

Measurement of Hadron and Lepton-Pair Production in e⁺e⁻ Collisions at $\sqrt{s} = 192 - 208$ GeV at LEP

L3 Collaboration

Abstract

Hadron production and lepton-pair production in e⁺e⁻ collisions are studied with data collected with the L3 detector at LEP at centre-of-mass energies $\sqrt{s} = 192 - 208$ GeV. Using a total integrated luminosity of 453 pb⁻¹, 36057 hadronic events and 12863 lepton-pair events are selected. The cross sections for hadron production and lepton-pair production are measured for the full sample and for events where no high-energy initial-state-radiation photon is emitted prior to the collisions. Lepton-pair events are further investigated and forward-backward asymmetries are measured. Finally, the differential cross sections for electron-positron pair-production is determined as a function of the scattering angle. An overall good agreement is found with Standard Model predictions.

Dedicated to the memory of Dr. Stephan Wynhoff

1 Introduction

The study of fermion-pair production in e^+e^- collisions constitutes an important part of the LEP scientific program. It allows a test of the Standard Model of electroweak interactions [1] at energies never achieved before. At the same time, the large rates of these processes and the simplicity of the final states provide a useful resource to control detector performance and calibration. In addition, fermion pairs constitute an irreducible background for many measurements and for the search for new physics beyond the Standard Model. Therefore, its production mechanism must be studied and controlled. Finally, LEP explores a new energy range above the Z resonance and possible deviations of fermion-pair production measurements from their precise theoretical expectations could give access to effects of new physics beyond the Standard Model at a scale too large to be directly observed.

This paper describes the study of fermion-pair production through the processes:

$$e^+e^- \rightarrow \text{hadrons}\,(\gamma)\,, \quad e^+e^- \rightarrow \mu^+\mu^-(\gamma)\,, \quad e^+e^- \rightarrow \tau^+\tau^-(\gamma) \ \text{and} \ e^+e^- \rightarrow e^+e^-(\gamma)\,,$$

where the symbol (γ) indicates the possible presence of additional photons. These reactions proceed through s-channel e^+e^- annihilation mediated by a photon or a Z boson. The $e^+e^- \rightarrow e^+e^-(\gamma)$ process receives additional contributions from t-channel exchange amplitudes, which increase for decreasing scattering angles, θ. The scattering angle is defined as the angle between the directions of the incoming electron and the outgoing fermion.

The L3 collaboration studied fermion-pair production at the Z resonance [2] and for centre-of-mass energies $\sqrt{s} = 130 \text{ GeV} - 189 \text{ GeV}$ [3,4]. This paper extends these studies to the high-energy and high-luminosity data sample collected at LEP at $\sqrt{s} = 191.6 \text{ GeV} - 209.2 \text{ GeV}$, corresponding to an integrated luminosity of 453 pb^{-1}. The study of the $e^+e^- \rightarrow \nu\bar{\nu}(\gamma)$ process is discussed in Reference 5. Measurements of hadron and lepton-pair production above the Z resonance were also performed by the other LEP collaborations [6].

For a substantial fraction of the events, initial-state-radiation (ISR) photons lower the initial centre-of-mass energy to an *effective* centre-of-mass energy, $\sqrt{s'}$. The case $\sqrt{s'} \approx m_Z$, where m_Z is the mass of the Z boson, is called *radiative return to the Z*. The value of s' can be computed from the sum of the energies of all ISR photons, E_γ, and of their momentum vectors, $\vec{P}_\gamma$, as:

$$s' = s - 2E_\gamma\sqrt{s} + E_\gamma^2 - \vec{P}_\gamma^{\,2}\,. \tag{1}$$

Events from fermion-pair production are divided into two categories: *inclusive* events and *high-energy* events. The former include radiative return to the Z. The latter comprises events with small ISR effects, where $\sqrt{s'} \approx \sqrt{s}$. The quantity $\sqrt{s'}$ is a natural choice to assign events to these two categories for s-channel processes. In the presence of t-channel contributions in the $e^+e^- \rightarrow e^+e^-(\gamma)$ process, the acollinearity angle, ζ, is a more appropriate choice. It is calculated as the complement to 180° of the angle between the directions of the final-state electrons. In the following, the criteria listed in Table 1 are used to assign events to the two classes. Measurements for the s-channel processes are performed in a limited fiducial volume and then extrapolated to the full angular region. Measurements for the $e^+e^- \rightarrow e^+e^-(\gamma)$ process are instead given in a limited angular region, with no extrapolation. Events with low values of $\sqrt{s'}$ in the s-channel processes and large values of ζ in the $e^+e^- \rightarrow e^+e^-(\gamma)$ process are excluded in order to obtain a high experimental signal-to-background ratio and reduce uncertainties on radiative corrections. Experimental uncertainties on the determination of $\sqrt{s'}$ and ζ introduce an additional background, due to event migration, denoted as ISR contamination.

	e$^+$e$^-$ →			
	hadrons (γ)	$\mu^+\mu^-(\gamma)$	$\tau^+\tau^-(\gamma)$	e$^+$e$^-(\gamma)$
Inclusive events	$\sqrt{s'} > 60$ GeV	$\sqrt{s'} > 75$ GeV		$\zeta < 120°$
High-energy events	$\sqrt{s'} > 0.85\sqrt{s}$			$\zeta < 25°$
ISR/FSR interference	Excluded			Included
Low-mass fermion pairs	Excluded			Included

Table 1: The signal definition: criteria used to classify events into the inclusive and high-energy samples and the channel-by-channel treatment of the interference of initial- and final-state radiation photons and additional low-mass fermion pairs.

The effective centre-of-mass energy is not well defined in presence of interference between initial- and final-state photon radiation. This effect is excluded from the signal definition for the e$^+$e$^-$ → hadrons (γ), e$^+$e$^-$ → $\mu^+\mu^-(\gamma)$ and e$^+$e$^-$ → $\tau^+\tau^-(\gamma)$ processes, as discussed in Reference 4. The signal definition for the e$^+$e$^-$ → e$^+$e$^-(\gamma)$ process includes effects of this interference.

Besides the emission of ISR photons, the production of initial-state fermion pairs could also lower the value of $\sqrt{s'}$. This effect was previously investigated and found to have a negligible impact on the selection efficiencies [4]. In the following, it is excluded from the signal definition of the e$^+$e$^-$ → hadrons (γ), e$^+$e$^-$ → $\mu^+\mu^-(\gamma)$ and e$^+$e$^-$ → $\tau^+\tau^-(\gamma)$ processes and included in the signal definition of the e$^+$e$^-$ → e$^+$e$^-(\gamma)$ process.

Table 1 summarises the treatment of the interference between initial- and final-state photon radiation and the production of initial-state fermion pairs for the different channels.

This paper presents results of the measurements of cross sections for hadron and lepton-pair production for both inclusive and high-energy events. The forward-backward asymmetries of lepton-pair production, A_{fb}, are studied for both the inclusive and the high-energy samples. Finally, electron-positron pair-production is further investigated and its differential cross sections as a function of the scattering angle, $\mathrm{d}\sigma/\mathrm{d}\cos\theta$, are measured for high-energy events.

For the high-energy sample, A_{fb} is defined through the parametrisation of the differential cross section:

$$\frac{1}{\sigma}\frac{\mathrm{d}\sigma}{\mathrm{d}\cos\theta} = \frac{3}{8}(1 + \cos^2\theta) + A_{\mathrm{fb}}\cos\theta + \frac{1}{\varepsilon(\cos\theta)\sigma}\int_{\sqrt{s'}}^{\sqrt{s}}\mathrm{d}m_{\mathrm{f\bar{f}}}\,\varepsilon(\cos\theta, m_{\mathrm{f\bar{f}}})\frac{\partial^2\sigma_{\mathrm{intf}}}{\partial\cos\theta\,\partial m_{\mathrm{f\bar{f}}}}\,, \quad (2)$$

where σ_{intf} is the contribution to the cross section from the interference between initial- and final-state photon radiation and ε is the efficiency as a one- or two-dimensional function of $\cos\theta$ and of the fermion-pair mass, $m_{\mathrm{f\bar{f}}}$. It is computed from Monte Carlo simulations. For the inclusive sample, ISR distorts the angular distribution such that the Born approximation of Equation (2) is not appropriate. Instead, for the e$^+$e$^-$ → $\mu^+\mu^-(\gamma)$ and the e$^+$e$^-$ → $\tau^+\tau^-(\gamma)$ processes, the forward-backward asymmetry is obtained from the differential cross section and extrapolated to the full solid angle using the ZFITTER program [7]. These corrections are about 2%. The forward-backward asymmetry of the e$^+$e$^-$ → e$^+$e$^-(\gamma)$ process is obtained by counting forward- and backward-scattered events in a given fiducial volume.

Section 2 describes the data sample and the measurement of the integrated luminosity. Section 3 describes the Monte Carlo simulation of signal and background processes as well as the theoretical predictions for fermion-pair production. The analysis methods and the event selections for the individual channels closely follow those used at lower centre-of-mass energies [4].

3

They are summarised, together with the results for cross sections and asymmetries and a discussion of the systematic uncertainties, in Section 4 for the $e^+e^- \to$ hadrons (γ) process, in Section 5 for the $e^+e^- \to \mu^+\mu^-(\gamma)$ process, in Section 6 for the $e^+e^- \to \tau^+\tau^-(\gamma)$ process and, finally, in Section 7 for the $e^+e^- \to e^+e^-(\gamma)$ process. Section 8 contains the summary and the conclusions.

2   Data sample

Data collected at LEP using the L3 detector [8–10] in the years 1999 and 2000 are investigated. In the year 1999, LEP was operated at four centre-of-mass energies between 191.6 GeV and 201.9 GeV which are treated separately in the following. In the year 2000, in order to enhance the discovery potential for the Standard Model Higgs boson, the LEP centre-of-mass energy was varied between 202.5 GeV and 209.2 GeV. These data are divided into three energy ranges. The seven average centre-of-mass energies considered in this analysis are listed in Table 2. The precise determination of the LEP centre-of-mass energy is discussed in Reference 11.

A total integrated luminosity of 453 pb^{-1} is considered. Its breakdown for the different values of $\sqrt{s}$ is given in Table 2 for the four final states under investigation. Differences between the channels are due to different data-quality requirements.

The integrated luminosity is measured using small-angle Bhabha scattering events recorded by two BGO calorimeters located close to the beam line on opposite sides of the interaction region, and collected by a dedicated trigger [10]. Events with two back-to-back energy clusters are selected and a tight fiducial volume cut, 34 mrad $< \theta <$ 54 mrad, $|90° - \phi| > 11.25°$ and $|270° - \phi| > 11.25°$ [1], is imposed on the coordinates of the highest-energy cluster. The highest-energy cluster on the opposite side should be contained in a larger fiducial volume, 32 mrad $< \theta <$ 65 mrad, $|90° - \phi| > 3.75°$ and $|270° - \phi| > 3.75°$.

Systematic uncertainties on the measurement of the integrated luminosity originate from the event selection criteria, the precise knowledge of the detector geometry and position, and the limited Monte Carlo statistics used to determine the selection efficiency. For 20% of the data collected in 2000, some trigger instabilities required the use of additional information from the cross section of hadron production in photon-photon collisions, resulting in a further systematic uncertainty. The total experimental systematic uncertainties for the years 1999 and 2000 are 0.14% and 0.18%, respectively. An additional theoretical uncertainty of 0.12% affects the determination of the integrated luminosity. These uncertainties are negligible with respect to the statistical and systematic uncertainties of the measurements described below.

3   Monte Carlo samples and theoretical predictions

The efficiencies and background levels of each selection, as well as some systematic uncertainties, are determined by means of Monte Carlo simulations. The following event generators are used: BHAGENE [12] and BHWIDE [13] for the $e^+e^- \to e^+e^-(\gamma)$ process; BHLUMI [14] for Bhabha scattering in the fiducial volume used in the determination of the integrated luminosity; TEEGG [15] for the $e^+e^- \to e^+e^-\gamma$ process where one fermion is close to the beam line and the photon in the detector; KK2f [16] for the $e^+e^- \to$ hadrons (γ), $e^+e^- \to \mu^+\mu^-(\gamma)$ and $e^+e^- \to \tau^+\tau^-(\gamma)$ processes; PYTHIA [17] for the $e^+e^- \to ZZ$ and $e^+e^- \to Ze^+e^-$ processes;

---

[1] The azimuthal angle, ϕ, is measured from an axis pointing toward the centre of the LEP ring.

KORALW [18] for W-boson pair production, $e^+e^- \rightarrow W^+W^-$; EXCALIBUR [19] for the four-fermion processes $e^+e^- \rightarrow q\bar{q}'e\nu$ and $e^+e^- \rightarrow e^+e^-e^+e^-$; GGG [20] for the $e^+e^- \rightarrow \gamma\gamma(\gamma)$ process; PHOJET [21] and DIAG36 [22] for hadron and lepton production in photon-photon collisions, $e^+e^- \rightarrow e^+e^-$hadrons and $e^+e^- \rightarrow e^+e^-\ell^+\ell^-$, respectively.

The hadronisation process is described with the PYTHIA Monte Carlo, whose parameters are tuned with data collected with the L3 detector at the Z resonance [23]. The HERWIG [24] and ARIADNE [25] Monte Carlo programs, also tuned on the same data [23], are used for systematic studies in the $e^+e^- \rightarrow$ hadrons channel.

Monte Carlo events are generated for each centre-of-mass energy. The L3 detector response is simulated using the GEANT [26] program which takes into account the effects of energy loss, multiple scattering and showering in the detector. The GHEISHA [27] package is used for the simulation of hadronic interactions. Time-dependent detector efficiencies, as monitored during the data-taking period, are included in the simulations. This "real-detector" simulation assures the control of the selection efficiencies. However, time-dependent second-order effect might escape the monitoring procedure and introduce a difference between data and the Monte Carlo description of some selection variables. The selection cuts described in the following are chosen so as to minimise these small discrepancies. The region of maximal discrimination between the signals and the backgrounds is scanned in a window of width several times the resolution of the selection variables. A value of the cut is retained for which the data and Monte Carlo differences are minimal. The observed differences are then retained as an estimation of systematic uncertainties on the detector modelling. These are discussed in detail in the following sections.

The measurements are compared to the predictions of the Standard Model as calculated using the ZFITTER [7] program for the $e^+e^- \rightarrow$ hadrons (γ), $e^+e^- \rightarrow \mu^+\mu^-(\gamma)$ and $e^+e^- \rightarrow \tau^+\tau^-(\gamma)$ processes and the TOPAZ0 [28] program for the $e^+e^- \rightarrow e^+e^-(\gamma)$ process. The following input parameters are used [29]: $m_Z = 91.1876 \pm 0.0021$ GeV, $m_t = 174.3 \pm 5.1$ GeV for the top-quark mass, $\alpha_s(m_Z^2) = 0.1187 \pm 0.0020$ for the strong coupling and $\Delta\alpha_{had}^{(5)} = 0.02763 \pm 0.00036$ for the hadronic contribution to the running of the electromagnetic coupling. The Higgs-boson mass is chosen as $m_H = 150^{+110}_{-36}$ GeV, compatible with the lower and higher mass limits of 114.4 GeV [30] and 285 GeV [31], respectively. The theoretical uncertainties on the Standard Model predictions are estimated to be below 1% except for the predictions for large-angle Bhabha scattering where they reach 1.5% [32]. The values of s' used in the calculations account for the energies of ISR photons through Equation (1), where E_γ and $\vec{P}_\gamma$ also include the four-momenta of low-mass fermion pairs. The stability of the predictions with respect to the Standard Model input parameters is checked by changing these within their uncertainties. The variations of the predictions are below 0.1%, resulting in a negligible additional systematic uncertainty.

4 The $e^+e^- \rightarrow$ hadrons (γ) process

4.1 Event selection

High-multiplicity events from the $e^+e^- \rightarrow$ hadrons (γ) process are selected in the fiducial volume of the L3 calorimeters, $|\cos\theta| < 0.995$ [4, 33]. These events are collected by redundant triggers based on the energy deposition in the calorimeters, the presence of pairs of back-to-back charged tracks in the tracker and the multiplicity of hits in the scintillator time-of-flight system. The overall trigger efficiency is measured from data to be close to 100%, with a negligible uncertainty.

Background from lepton-pair production is rejected by requiring the event to have at least 12 calorimetric clusters. Background from hadron production in photon-photon collisions is reduced by two criteria: the hadronic energy calculated by excluding isolated clusters, E_{had}, must be greater than $0.4\sqrt{s}$ and the longitudinal energy-imbalance must be less than $0.8E_{\text{tot}}$, where E_{tot} is the total energy reconstructed in the detector. Events from W-boson pair production with semi-leptonic decay are removed by requiring the transverse energy-imbalance to be less than $0.3E_{\text{tot}}$. Hadronic decays of W bosons are reduced by applying the JADE algorithm [34] with a resolution parameter $y_{\text{cut}} = 0.01$ and removing events with at least four jets, each with an energy greater than 15 GeV.

Two methods are used to derive the four-momentum of ISR photons and calculate $\sqrt{s'}$ through Equation (1). The first method uses a kinematic fit assuming the emission of either zero, one, or two photons along the beam line. The hypothesis which best fits the data is retained and the photon four-momenta are derived from the fit. In the second method, each event is clustered into two jets using the JADE algorithm. A single photon is assumed to be emitted along the beam line and its energy is estimated from the reconstructed polar angles of the jets, θ_1 and θ_2, as:

$$E_\gamma = \sqrt{s}\frac{|\sin(\theta_1 + \theta_2)|}{\sin\theta_1 + \sin\theta_2 + |\sin(\theta_1 + \theta_2)|}. \tag{3}$$

In about 15% of selected events, an isolated high-energy cluster is detected in the electromagnetic calorimeter. It is assumed to be an ISR photon, and its energy and momentum are added to those determined by either method before applying Equation (1).

The first method is used to derive the following results, while the second is used as a cross check and to assess the systematic uncertainty on the $\sqrt{s'}$ determination.

Figure 1a shows the distributions for data and Monte Carlo of $E_{\text{had}}/\sqrt{s}$ for the full data sample. The three peaks correspond, from left to right, to hadron production in photon-photon collisions, to the radiative return to the Z and to high-energy events. Figure 2a shows the data and Monte Carlo distributions of the values of $\sqrt{s'}$ reconstructed with the second method for $\sqrt{s} = 207$ GeV. The two peaks correspond to the radiative return to the Z and to high-energy events.

Selection efficiencies and background contributions for the different values of $\sqrt{s}$ are listed in Tables 3 and 4 for the inclusive and high-energy samples, respectively. The largest residual backgrounds are from W-boson pair production, hadron production in photon-photon collisions and, for the high-energy sample, ISR contamination. Other minor sources of background are tau-pair production and four-fermion events from Z-boson pair production and the $e^+e^- \rightarrow Ze^+e^-$ process.

4.2   Results

The numbers of observed events and the measurements of the cross sections of the $e^+e^- \rightarrow$ hadrons (γ) process for the inclusive and high-energy samples are presented in Table 5, together with their statistical and systematic uncertainties. The corresponding Standard Model predictions are also given. Figure 3 compares the cross section measurements to the Standard Model predictions. Good agreement is observed.

A χ^2 test of the compatibility of data and Standard Model prediction yields values of $\chi^2/\text{d.o.f.}$ of 1.4 and 0.7 for the inclusive and high-energy samples, respectively. These and all following calculations of $\chi^2/\text{d.o.f.}$ include only statistical uncertainties.

4.3 Systematic uncertainties

The statistical uncertainty on the cross sections of the $e^+e^- \rightarrow$ hadrons (γ) process varies between 1.1% and 2.1% for the inclusive sample and 2.5% and 4.6% for the high-energy sample, depending on $\sqrt{s}$, with the exclusion of the low-luminosity highest-energy point. The overall systematic uncertainties for the inclusive sample are comparable to the statistical uncertainties, at about 1.1%, while for the high-energy sample, with a value of about 0.8%, they are less than a third of the statistical uncertainties [4, 33].

The systematic uncertainty on the hadronisation process, which amounts to 0.47% for the inclusive sample and 0.63% for the high-energy sample, is derived by using the HERWIG and ARIADNE Monte Carlo programs instead of the default PYTHIA Monte Carlo. The analysis is repeated by using these alternative Monte Carlo simulations. Their average is calculated and half of its difference with respect to the original measurement is assigned as systematic uncertainty. Limited signal and background Monte Carlo statistics imply systematic uncertainties of $0.07 - 0.17\%$ and $0.14 - 0.50\%$ for the inclusive and high-energy samples, respectively, depending on the centre-of-mass energy. The systematic uncertainty from calorimeter calibration, which amounts to 0.48% for the inclusive sample and 0.26% for the high-energy sample, is assessed by repeating the analysis changing the calorimeter calibration constants within the uncertainties of their determination from Z-peak data. The Monte Carlo treatment of the interference between initial- and final-state radiation contributes systematic uncertainties of 0.10% and 0.20% for the inclusive and high-energy samples, respectively. The $\sqrt{s'}$ reconstruction uncertainty is estimated from the differences of the cross sections obtained with each of the two methods as 0.36% for the inclusive sample and 0.15% for the high-energy sample. The impact of the event-selection procedure is studied by varying the selection criteria, in order to assess the effects of possible discrepancies between data and the Monte Carlo simulation, and by using a different strategy to remove events from W-boson pair production. Uncertainties of 0.22% and 0.07% are obtained for the inclusive and high-energy samples, respectively. Uncertainties in the modelling of hadron production in photon-photon interactions propagate to a systematic uncertainty of 0.05% for both the inclusive and high-energy samples. For the cross section measurement of the high-energy sample, three quarters of the systematic uncertainty is correlated between energy points.

5 The $e^+e^- \rightarrow \mu^+\mu^-(\gamma)$ process

5.1 Event selection

Muon-pair candidates are selected from low-multiplicity events with two identified muons [4,35]. These events are mainly collected by a trigger based on several possible combinations of tracks in different regions of the muon spectrometer. The trigger efficiency is enhanced by including events with back-to-back tracks in the central tracker and events with isolated photons in the calorimeters, susceptible to originate from ISR. The combined trigger efficiency is determined from data and varies between 97.8% and 99.9%, according to the data-taking conditions, with statistical uncertainties between 0.1% and 0.8%.

The muon candidates are required to have at least two track-segments reconstructed in the fiducial volume, $|\cos\theta| < 0.9$, of the muon spectrometer. In addition, for 15% of the events, only one muon is identified in the muon spectrometer while the other is reconstructed from the signature of a minimum-ionising particle in the calorimeters matched to a track in the central

tracker and, possibly, a single track-segment in the muon spectrometer.

Background from lepton-pair production in photon-photon collisions and from tau-pair production is suppressed by requiring the momentum of the most energetic muon, p_{max}, to satisfy $p_{max} > 0.4 E_{beam}$, where E_{beam} is the beam energy. These backgrounds are further removed by requiring the acollinearity angle to be less than $90°$. Background from cosmic rays is rejected by three criteria: at least one of the muons must originate from the interaction point; at least one of the muons must have a signal in the scintillator time-of-flight system in time with the beam crossing; finally, if both muons have such a scintillator hit, these must be simultaneous. The residual background from cosmic rays is estimated from complementary subsamples of data.

The value of $\sqrt{s'}$ is derived from Equation (1). If one or more isolated high-energy photons are detected in the event, their energies are directly used. If no such photons are detected, the hypothesis that a single ISR photon is emitted along the beam line is made, and Equation (3) is used to derive its energy from the muon polar angles.

Figure 1b shows the distribution for data and Monte Carlo of p_{max}/E_{beam} for the full data sample, while Figure 2b shows the distributions of $\sqrt{s'}$ reconstructed at $\sqrt{s} = 207$ GeV.

Selection efficiencies and background contributions are listed in Tables 3 and 4 for the inclusive and high-energy samples, respectively. The largest residual backgrounds are from lepton-pair production in photon-photon collisions, W-boson pair production and, for the high-energy sample, ISR contamination. Other minor sources of background are tau-pair production, Z-boson pair production and cosmic rays.

5.2   Results

The numbers of observed events and the measurements of the cross sections of the $e^+e^- \rightarrow \mu^+\mu^-(\gamma)$ process for the inclusive and high-energy samples are presented in Table 5, together with their statistical and systematic uncertainties. The corresponding Standard Model predictions are also given. Figure 4a compares the measured cross section for the inclusive and high-energy samples with the Standard Model predictions as a function of $\sqrt{s}$. Good agreement is observed, with values of $\chi^2/$d.o.f. of 1.9 and 1.4 for the inclusive and high-energy samples, respectively.

The forward-backward asymmetry is determined for the inclusive and high-energy samples with the results presented in Table 6, together with the numbers of events selected in the forward and backward hemispheres. The determination of A_{fb} takes into account both the charge confusion per event, measured in data to be between 0.2% and 0.5%, and the asymmetries induced by the accepted background. Figure 4b presents the values of A_{fb} measured as a function of $\sqrt{s}$. They are in good agreement with the Standard Model predictions, also shown, with values of $\chi^2/$d.o.f. of 0.2 and 0.8 for the inclusive and high-energy samples, respectively.

5.3   Systematic uncertainties

For the high-energy sample, the systematic uncertainties on the measurement of the $e^+e^- \rightarrow \mu^+\mu^-(\gamma)$ cross sections and forward-backward asymmetries are in the ranges $2.7 - 4.0\%$ and $3.4 - 10\%$, respectively [4, 35], depending on $\sqrt{s}$. These uncertainties are at least three times smaller than the corresponding statistical uncertainties.

The limited signal and background Monte Carlo statistics imply systematic uncertainties of $1.8 - 3.0\%$ and $2.4 - 5.5\%$, depending on $\sqrt{s}$, for the cross section and A_{fb} measurements, respectively. The uncertainty in detector modelling, assessed by varying the selection criteria,

is dominated by the simulation of p_{max} and the control of the fiducial volume. Depending on the running conditions and the detector ageing, this uncertainty varies between 1.7% and 2.4% for the cross sections and 1.0% and 7.0% for A_{fb}. The uncertainty on the trigger efficiency has a small impact on the cross section with a systematic uncertainty between 0.2% and 0.8%, depending on the year of data taking. The charge confusion per event has a relative uncertainty of about 20%, which results in a small additional uncertainty on A_{fb}, of about 0.2%.

For the high-energy measurement of the cross sections, between one third and half of the systematic uncertainty is correlated between the energy points. For the asymmetries, these figures increase to one half and two thirds.

6 The $e^+e^- \rightarrow \tau^+\tau^-(\gamma)$ process

6.1 Event selection

Tau candidates are identified in the fiducial volume $|\cos\theta| < 0.94$ as narrow, low multiplicity, jets containing at least one charged particle [4,36]. Several classes of triggers collect these events with an efficiency, measured from data, close to 100% with a negligible uncertainty: low- and large-angle charged-track triggers, the muon triggers, a scintillator time-of-flight multiplicity trigger and calorimeter-based energy triggers.

Events with two tau candidates are selected. If both jets contain electrons[2] or muons the events are rejected. The momentum of the most energetic tau jet, p_1, is estimated from its polar angle, θ_1, and the polar angle of the other tau jet, θ_2, imposing energy and momentum conservation as:

$$p_1 = \sqrt{s}\frac{\sin\theta_2}{\sin\theta_1 + \sin\theta_2 + \sin(\theta_1 + \theta_2)} \ . \tag{4}$$

The momentum of the other tau jet is estimated analogously. Background from hadronic events is removed by requiring at most 16 calorimetric clusters and at most 9 tracks in the central tracker. Residual background from the $e^+e^- \rightarrow e^+e^-(\gamma)$ process is suppressed by requiring that the energies of the most energetic and the second most energetic electromagnetic cluster in the event are less than 85% and 50% of the estimated momenta of the corresponding tau jets. Similarly, background from muon-pair production is further reduced by requiring the momentum of each muon in the event to be less than 85% of the estimated momentum of the corresponding tau jet. Background from photon-photon collisions is reduced by requiring the most energetic jet to have an energy E_{max} such that $E_{\mathrm{max}} > 0.275p_1$. Leptonic final states from W-boson pair production are rejected by requiring the acollinearity angle to be less than 15°. Background from cosmic rays is suppressed using information from the time-of-flight system and by requiring any muons in the event to originate from the interaction point.

The value of $\sqrt{s'}$ is derived from Equation (1) by using the four-momenta of all detected isolated high-energy photons. If the event contains no such photons, the energy of a single ISR photon directed along the beam line is calculated from the tau-jet polar angles with Equation (3).

Figure 1c shows the data and Monte Carlo distributions of E_{max}/p_1 for the full data sample, while Figure 2c shows the distributions of $\sqrt{s'}$ reconstructed at $\sqrt{s} = 207$ GeV.

The charge of the tau candidates is determined from the sum of the charges of the tracks constituting the jets or of the identified electrons or muons. Only event with an unambiguous

---

[2] Here and in the following, the term "electron" denotes both electrons and positrons.

charge assignment are retained for the study of A_{fb}. These comprise 72% of the inclusive sample and 75% of the high-energy sample.

Tables 3 and 4 list the selection efficiencies and background contributions for the inclusive and high-energy samples, respectively. The largest residual backgrounds are from tau production in photon-photon collisions and other sources such as the $e^+e^- \rightarrow e^+e^-(\gamma)$ process, muon-pair production and W-boson pair production. ISR contamination contributes to the background to the high-energy sample.

6.2 Results

The numbers of observed events and the measurements of the cross sections of the $e^+e^- \rightarrow \tau^+\tau^-(\gamma)$ process for the inclusive and high-energy samples are presented in Table 5, together with their statistical and systematic uncertainties. The measurements are compared in Figure 4a with the Standard Model predictions as a function of $\sqrt{s}$. All measurements are in good agreement with the Standard Model predictions: $\chi^2/\mathrm{d.o.f.}$ of 0.3 and 0.5 are observed for the inclusive and high-energy cross sections, respectively.

The forward-backward asymmetry is determined for the inclusive and high-energy samples with the results presented in Figure 4b and Table 6, which also lists the numbers of events selected in the forward and backward hemispheres. The determination of A_{fb} takes into account the charge confusion per event, measured in data, which is of the order of 2%. Good agreement with the Standard Model predictions is found, with values of $\chi^2/\mathrm{d.o.f.}$ of 0.8 and 0.9 for the inclusive and high-energy sample, respectively.

6.3 Systematic uncertainties

For the high-energy sample, the systematic uncertainties on the measurement of the $e^+e^- \rightarrow \tau^+\tau^-(\gamma)$ cross sections and forward-backward asymmetries are $2.0 - 3.4\%$ and $9.6 - 17\%$, depending on the centre-of-mass energy and excluding the highest-energy point, respectively [4, 36]. These uncertainties are considerably lower than the corresponding statistical uncertainties.

The main systematic uncertainties on the cross section determination are the detector modelling and the limited signal and background Monte Carlo statistics. The former, of 1.4%, receives equal contributions from the simulation of the variables used for background rejection on the basis of calorimetric information and from the control of the fiducial volume. The limited Monte Carlo statistics implies systematic uncertainties of $1.4 - 3.1\%$, depending on $\sqrt{s}$.

The systematic uncertainties on A_{fb} are dominated by the limited Monte Carlo statistics, with an additional contribution of about 3.0% from the detector modelling. The charge confusion per event is determined with a relative uncertainty up to 50%, which has a negligible contribution to the systematic uncertainties.

The systematic uncertainties on the high-energy measurements of the cross sections and asymmetries are mostly uncorrelated between the energy points.

7 The $e^+e^- \rightarrow e^+e^-(\gamma)$ process

7.1 Event selection

Electron candidates are identified as clusters in the BGO electromagnetic calorimeter in the range $|\cos\theta| < 0.98$ [4, 37]. Two triggers collect these events: a charged-track trigger which re-

quires two back-to-back tracks and a calorimeter-based energy trigger. The combined efficiency of the two triggers, measured from the data, is close to 100%, with a negligible uncertainty, for $|\cos\theta| < 0.72$ and is $99.0 \pm 0.1\%$ for $|\cos\theta| < 0.98$.

The electron-candidate clusters must be associated with tracks which contain at least 20% of the expected number of hits in a three-degree azimuthal wedge around the electron direction. Backgrounds from tau-pair production, lepton production in photon-photon collisions and fully-leptonic decays of W-boson pairs are removed by selection criteria on the energy of the clusters. For the barrel region, $|\cos\theta| < 0.72$, the energy of the most energetic cluster must satisfy $E_1 > 0.5E_{\mathrm{beam}}$, while the energy of the other cluster must satisfy $E_2 > 20$ GeV. For the endcap regions, $0.81 < |\cos\theta| < 0.98$, these criteria are relaxed to $E_1 > 0.4E_{\mathrm{beam}}$ and $E_2 > 10$ GeV. Events with clusters in the region between the BGO barrel and either one of the BGO endcaps, $0.72 < |\cos\theta| < 0.81$, instrumented with a lead and scintillating-fibre calorimeter [9], are rejected.

The absolute value of the cosine of the centre-of-mass scattering angle, $|\cos\theta^\star|$, is determined from the polar angles of the electron candidates as:

$$|\cos\theta^\star| \equiv \frac{|\sin\theta_1 - \theta_2|}{\sin\theta_1 + \sin\theta_2}.$$

(5)

Only events in the fiducial volume $|\cos\theta| < 0.72$ are used to measure the cross section and A_{fb}, while the measurement of the differential cross section covers the fiducial volume $|\cos\theta^\star| < 0.9$.

Figure 1d shows the data and Monte Carlo distributions of E_1/E_{beam} for the full data sample, while Figure 2d presents the ζ distribution for $\sqrt{s} = 207$ GeV.

Selection efficiencies and background contributions are listed in Tables 3 and 4 for the inclusive and high-energy samples, respectively. The largest residual backgrounds are from tau-pair production and W-boson pair production. Minor sources of background are electron production in photon-photon collisions, and the $\mathrm{e}^+\mathrm{e}^- \to \mathrm{e}^+\mathrm{e}^-\gamma$, $\mathrm{e}^+\mathrm{e}^- \to \mathrm{Ze}^+\mathrm{e}^-$ and $\mathrm{e}^+\mathrm{e}^- \to \gamma\gamma(\gamma)$ processes. ISR contamination is negligible.

7.2 Results

Table 5 presents the numbers of observed events and the measurements of the cross sections of the $\mathrm{e}^+\mathrm{e}^- \to \mathrm{e}^+\mathrm{e}^-(\gamma)$ process for the inclusive and high-energy samples for $|\cos\theta| < 0.72$, together with their statistical and systematic uncertainties. Figure 5a compares these cross sections with Standard Model predictions. Good agreement is observed with $\chi^2/\mathrm{d.o.f.}$ of 1.4 and 1.3 for the inclusive and high-energy samples, respectively.

Table 7, continued in Table 8, presents the differential cross section as a function of $|\cos\theta^\star|$, together with the numbers of observed events and the background fractions, along with the selection efficiencies for the high-energy sample. Only events with $|\cos\theta^\star| < 0.9$ are considered. The differential cross section is compared in Figure 6 to the Standard Model predictions of the BHWIDE Monte Carlo, also given in Tables 7 and 8. Good agreement is found with $\chi^2/\mathrm{d.o.f.} = 1.0$.

The measured values of the forward-backward asymmetry are listed in Table 6, together with the numbers of events selected in the forward and backward hemispheres. This measurements include a correction for the charge confusion per event, estimated from data, which varies between 4.5% and 8.9% according to the polar angle. A comparison with Standard Model predictions, also listed in Table 6 and presented in Figure 5b, shows good agreement, with $\chi^2/\mathrm{d.o.f.}$ of 1.4 and 1.1 for the inclusive and high-energy samples, respectively.

7.3 Systematic uncertainties

The systematic uncertainties on the $e^+e^- \to e^+e^-(\gamma)$ cross sections and A_{fb} are between a factor two and five smaller than the corresponding statistical uncertainties [4,37]. Excluding the luminosity-limited highest centre-of-mass energy, statistical uncertainties on the cross sections of $2.0-3.8\%$ and $2.0-4.0\%$ are observed for the inclusive and high-energy samples, respectively, while systematic uncertainties are about 1.3% and 0.5%, respectively. The high-energy asymmetry is measured with a statistical precision of $2.0 - 4.0\%$, depending on the centre-of-mass energy, while its systematic uncertainty is about 1%.

The systematic uncertainties on the high-energy cross sections and A_{fb} are dominated by the modelling of the tracker response and of edge effects in the control of the fiducial volume, 0.43%. Another important contribution arises from the limited signal, $0.19 - 0.31\%$, and background, 0.30%, Monte Carlo statistics. The simulation of the calorimeter response for the most-energetic electron contributes 0.13% to the total systematic uncertainty while the simulation of the least-energetic electron contributes 0.15%. The systematic uncertainty on A_{fb} contains an additional contribution of about 0.1% arising from the relative uncertainty on the charge-confusion, determined in data as $17 - 24\%$.

The determination of the differential cross section is also limited by the statistical uncertainties. It has the same sources of systematic uncertainty discussed above. At $\sqrt{s} = 207$ GeV, the detector modelling and control of the fiducial volume contributes $0.2-1.5\%$ and the limited background Monte Carlo statistics contributes $0.2 - 3.3\%$, depending on the polar angle. The effect of the limited signal Monte Carlo statistics raises to $0.5 - 8.1\%$, depending on the polar angle. While the overall increase of this source is due to the increased number of bins in which the Monte Carlo is divided, the largest amount corresponds to the region $0.72 < |\cos\theta^\star| < 0.81$, where some extrapolation factors account for the transition region between the barrel and end-cap BGO calorimeters which is not used to identify electrons.

The systematic uncertainties on the high-energy measurements of the cross sections and asymmetries are mostly correlated between the energy points. For the measurements of the differential cross sections, systematic uncertainties are mostly uncorrelated between energy points and between different angular ranges.

8 Summary and conclusions

A detailed study of the properties of fermion-pair production in e^+e^- collisions at LEP has been performed. The cross sections for hadron and lepton-pair production, as well as the forward-backward asymmetries for lepton-pair production, are measured both for the inclusive and high-energy samples. In addition, the high-energy samples of electron-positron pair-production are used to measure the differential cross sections as a function of the scattering angle.

These results are summarised in Figures $3-6$ and Tables $5-8$ together with their statistical and systematic uncertainties. To a good approximation, systematic uncertainties are not correlated between the different final states, both for the cross section measurements and for the measurements of the forward-backward asymmetries.

The global agreement of the results presented in this paper with the Standard Model expectations is presented in Figure 7. The 119 measurements of total and differential cross sections and of forward-backward asymmetries for the high-energy samples are considered. For each measurement, its difference with respect to the Standard Model expectation is plotted, divided by the statistical uncertainty. An excellent agreement with the expected Gaussian statistical

spread of the measurements is observed.

The results on the $e^+e^- \rightarrow e^+e^-(\gamma)$ process give access to the evolution of the electromagnetic coupling with the momentum transfer, whose measurement is discussed in a companion letter [38]. These measurements allow a search for manifestations of new physics at a scale which would not be directly detected at LEP [39].

These data complete the picture of fermion-pair production at LEP at $\sqrt{s} = 90$ GeV − 209 GeV: Figures 8−14 combine the results of this paper and of previous studies [2–4] to present the cross sections and forward-backward asymmetries measured with the L3 detector. Over the whole energy range explored at LEP, the measurements are well described by the predictions of the Standard Model.

References

[1] S.L. Glashow Nucl. Phys. **22** (1961) 579;
S. Weinberg, Phys. Rev. Lett. **19** (1967) 1264;
A. Salam, in *Elementary Particle Theory*, ed. N. Svartholm, Stockholm, Almquist & Wiksell (1968) 367;
M. Veltman, Nucl. Phys. **B7** (1968) 637;
G.M. 't Hooft, Nucl. Phys. **B35** (1971) 167;
G.M. 't Hooft and M. Veltman, Nucl. Phys. **B44** (1972) 189;
G.M. 't Hooft and M. Veltman, Nucl. Phys. **B50** (1972) 318.

[2] L3 Collab., M. Acciarri *et al.*, Eur. Phys. Jour. **C 16** (2000) 1.

[3] L3 Collab., M. Acciarri *et al.*, Phys. Lett. **B 370** (1996) 195;
L3 Collab., M. Acciarri *et al.*, Phys. Lett. **B 407** (1997) 361.

[4] L3 Collab., M. Acciarri *et al.*, Phys. Lett. **B 479** (2000) 101.

[5] L3 Collab., P. Achard *et al.*, Phys. Lett. **B 587** (2004) 16.

[6] ALEPH Collab., R. Barate *et al.*, Eur. Phys. Jour. **C 12** (2000) 183;
DELPHI Collab., P. Abreu *et al.*, Preprint hep-ex/0512012 (2005);
OPAL Collab., G. Abbiendi *et al.*, Eur. Phys. Jour. **C 33** (2004) 173;
and references therein.

[7] ZFITTER version 6.36 is used;
D. Bardin *et al.*, preprint hep-ph/9908433;
D. Bardin *et al.*, Z. Phys. **C 44** (1989) 493;
D. Bardin *et al.*, Nucl. Phys. **B 351** (1991) 1;
D. Bardin *et al.*, Phys. Lett. **B 255** (1991) 290.
For comparison with our measurements the cuts of Table 1 are applied to possible additional fermion pairs and the following flags are changed from the default values: `AFMT` = 1, `ALEM` = 2, `AMT4` = 5, `BOXD` = 2, `FBHO` = 1, `FINR` = 0, `FUNA` = 1, `INTF` = 0 and `PART` = 1.

[8] L3 Collab., B. Adeva *et al.*, Nucl. Inst. Meth. **A 289** (1990) 35;
L3 Collab., O. Adriani *et al.*, Physics Reports **236** (1993) 1;
M. Acciarri *et al.*, Nucl. Inst. Meth. **A 351** (1994) 300;
M. Chemarin *et al.*, Nucl. Inst. Meth. **A 349** (1994) 345;

A. Adam *et al.*, Nucl. Inst. Meth. **A 383** (1996) 342;
F. Beissel *et al.*, Nucl. Inst. Meth. **A 332** (1993) 33.

[9] G. Basti *et al.*, Nucl. Inst. Meth. **A 374** (1996) 293.

[10] I.C. Brock *et al.*, Nucl. Inst. Meth. **A 381** (1996) 236.

[11] R. Assmann *et al.*, Eur. Phys. J. **C 39** (2005) 253.

[12] BHAGENE version 3 is used;
J.H. Field, Phys. Lett. **B 323** (1994) 432;
J.H. Field and T. Riemann, Comp. Phys. Comm. **94** (1996) 53.

[13] BHWIDE version 1.01 is used;
S. Jadach *et al.*, Phys. Lett. **B 390** (1997) 298.

[14] BHLUMI version 4.04 is used;
S. Jadach *et al.*, Comp. Phys. Comm. **102** (1997) 229.

[15] TEEGG version 7.1 is used;
D. Karlen, Nucl. Phys. **B 289** (1987) 23.

[16] KK2f versions 4.14 and 4.19 are used;
S. Jadach *et al.*, Comp. Phys. Comm. **130** (2000) 260;
S. Jadach *et al.*, Phys. Rev. **D 63** (2001) 113009.

[17] PYTHIA versions 5.722 and 6.1 are used;
T. Sjöstrand *et al.*, Comp. Phys. Comm. **135** (2001) 238.

[18] KORALW version 1.513 is used;
S. Jadach *et al.*, Comp. Phys. Comm. **119** (1999) 272.

[19] EXCALIBUR version 1.11 is used;
R. Kleiss and R. Pittau, Comp. Phys. Comm. **83** (1994) 141.

[20] GGG version 2.03 is used;
F.A. Berends and R. Kleiss, Nucl. Phys. **B 186** (1981) 22.

[21] PHOJET version 1.05 is used.
R. Engel, Z. Phys. **C 66** (1995) 203;
R. Engel and J. Ranft, Phys. Rev. **D 54** (1996) 4244.

[22] DIAG36 version 2.06 is used;
F.A. Berends, P.H. Daverfeldt and R. Kleiss, Nucl. Phys. **B 253** (1985) 441.

[23] L3 Collaboration, P. Achard *et al.*, Phys. Rep. **399** (2004) 71.

[24] HERWIG version 6.202 is used;
G. Marchesini *et al.*, Comp. Phys. Comm. **67** (1992) 465;
G. Corcella *et al.*, JHEP **101** (2001) 010.

[25] ARIADNE version 4.12 is used;
L. Lönnblad, Comp. Phys. Comm. **71** (1992) 15.

[26] GEANT Version 3.15 is used;
R. Brun *et al.*, preprint CERN-DD/EE/84-1, revised 1987.

[27] H. Fesefeldt, RWTH Aachen, report PITHA 85/02 (1985).

[28] TOPAZ0 version 4.4 is used;
G. Montagna *et al.*, Nucl. Phys. **B401** (1993) 3;
G. Montagna *et al.*, Comp. Phys. Comm. **76** (1993) 328.

[29] S. Eidelman *et al.*, Phys. Lett. **B 592** (2004) 1.

[30] ALEPH Collab., DELPHI Collab., L3 Collab., OPAL Collab. and the LEP Working Group
for Higgs Boson Searches, Phys. Lett. **B 565** (2003) 61.

[31] The ALEPH, DELPHI, L3, OPAL, SLD Collaborations, the LEP Electroweak Working
Group, the SLD Electroweak and Heavy Flavour Groups, preprint hep-ex/0509008 (2005).

[32] M. Kobel *et al.*, *Two-fermion production in electron positron collisions*, CERN Report
2000-009, 2000, p. 292, hep-ph/0007180; and references therein.

[33] Jessica Hirschfelder, *Quark Pair Production in Electron-Positron Collisions at* $192 -
208$ *GeV*, Ph.D. thesis, Carnegie Mellon University, 2003.

[34] JADE Collab., W. Bartel *et al.*, Z. Phys. **C 33** (1986) 23;
JADE Collab., S. Bethke *et al.*, Phys. Lett. **B 213** (1988) 235.

[35] Alessandro De Salvo, *Dimuon production in* e^+e^- *collisions with the L3 experiment at
LEP2 up to the highest energies*, Ph.D. thesis, ETH Zurich, 2002.

[36] Sandra Muijs, *Tau Pair Production Above the Z Resonance*, Ph.D. thesis, Nijmegen University, 2001.

[37] Patrick Deglon, *Étude de la diffusion Bhabha avec le détecteur L3 au LEP*, Ph.D. thesis,
Geneva University, 2002.

[38] L3 Collab., P. Achard *et al.*, Phys. Lett. **B 623** (2005) 23.

[39] L3 Collab., P. Achard *et al.*, *Search for Manifestations of New Physics in Hadron and
Lepton-Pair Production at LEP*, in preparation.

The L3 Collaboration:

P.Achard[20] O.Adriani[17] M.Aguilar-Benitez[25] J.Alcaraz[25] G.Alemanni[23] J.Allaby[18] A.Aloisio[29] M.G.Alviggi[29] H.Anderhub[49] V.P.Andreev[6,34] F.Anselmo[8] A.Arefiev[28] T.Azemoon[3] T.Aziz[9] P.Bagnaia[39] A.Bajo[25] G.Baksay[26] L.Baksay[26] S.V.Baldew[2] S.Banerjee[9] Sw.Banerjee[4] A.Barczyk[49,47] R.Barillère[18] P.Bartalini[23] M.Basile[8] N.Batalova[46] R.Battiston[33] A.Bay[23] F.Becattini[17] U.Becker[13] F.Behner[49] L.Bellucci[17] R.Berbeco[3] J.Berdugo[25] P.Berges[13] B.Bertucci[33] B.L.Betev[49] M.Biasini[33] M.Biglietti[29] A.Biland[49] J.J.Blaising[4] S.C.Blyth[35] G.J.Bobbink[2] A.Böhm[1] L.Boldizsar[12] B.Borgia[39] S.Bottai[17] D.Bourilkov[49] M.Bourquin[20] S.Braccini[20] J.G.Branson[41] F.Brochu[4] J.D.Burger[13] W.J.Burger[33] X.D.Cai[13] M.Capell[13] G.Cara Romeo[8] G.Carlino[29] A.Cartacci[17] J.Casaus[25] F.Cavallari[39] N.Cavallo[36] C.Cecchi[33] M.Cerrada[25] M.Chamizo[20] Y.H.Chang[44] M.Chemarin[24] A.Chen[44] G.Chen[7] G.M.Chen[7] H.F.Chen[22] H.S.Chen[7] G.Chiefari[29] L.Cifarelli[40] F.Cindolo[8] I.Clare[13] R.Clare[38] G.Coignet[4] N.Colino[25] S.Costantini[39] B.de la Cruz[25] S.Cucciarelli[33] R.de Asmundis[29] P.Déglon[20] J.Debreczeni[12] A.Degré[4] K.Dehmelt[26] K.Deiters[47] D.della Volpe[29] E.Delmeire[20] P.Denes[37] F.DeNotaristefani[39] A.De Salvo[49] M.Diemoz[39] M.Dierckxsens[2] C.Dionisi[39] M.Dittmar[49] A.Doria[29] M.T.Dova[10,♯] D.Duchesneau[4] M.Duda[1] B.Echenard[20] A.Eline[18] A.El Hage[1] H.El Mamouni[24] A.Engler[35] F.J.Eppling[13] P.Extermann[20] M.A.Falagan[25] S.Falciano[39] A.Favara[32] J.Fay[24] O.Fedin[34] M.Felcini[49] T.Ferguson[35] H.Fesefeldt[1] E.Fiandrini[33] J.H.Field[20] F.Filthaut[31] P.H.Fisher[13] W.Fisher[37] G.Forconi[13] K.Freudenreich[49] C.Furetta[27] Yu.Galaktionov[28,13] S.N.Ganguli[9] P.Garcia-Abia[25] M.Gataullin[32] S.Gentile[39] S.Giagu[39] Z.F.Gong[22] G.Grenier[24] O.Grimm[49] M.W.Gruenewald[16] M.Guida[40] V.K.Gupta[37] A.Gurtu[9] L.J.Gutay[46] D.Haas[5] D.Hatzifotiadou[8] T.Hebbeker[1] A.Hervé[18] J.Hirschfelder[35] H.Hofer[49] M.Hohlmann[26] G.Holzner[49] S.R.Hou[44] B.N.Jin[7] P.Jindal[14] L.W.Jones[3] P.de Jong[2] I.Josa-Mutuberría[25] M.Kaur[14] M.N.Kienzle-Focacci[20] J.K.Kim[43] J.Kirkby[18] W.Kittel[31] A.Klimentov[13,28] A.C.König[31] M.Kopal[46] V.Koutsenko[13,28] M.Kräber[49] R.W.Kraemer[35] A.Krüger[48] A.Kunin[13] P.Ladron de Guevara[25] I.Laktineh[24] G.Landi[17] M.Lebeau[18] A.Lebedev[13] P.Lebrun[24] P.Lecomte[49] P.Lecoq[18] P.Le Coultre[49] J.M.Le Goff[18] R.Leiste[48] M.Levtchenko[27] P.Levtchenko[34] C.Li[22] S.Likhoded[48] C.H.Lin[44] W.T.Lin[44] F.L.Linde[2] L.Lista[29] Z.A.Liu[7] W.Lohmann[48] E.Longo[39] Y.S.Lu[7] C.Luci[39] L.Luminari[39] W.Lustermann[49] W.G.Ma[22] L.Malgeri[18] A.Malinin[28] C.Maña[25] J.Mans[37] J.P.Martin[24] F.Marzano[39] K.Mazumdar[9] R.R.McNeil[6] S.Mele[18,29] L.Merola[29] M.Meschini[17] W.J.Metzger[31] A.Mihul[11] H.Milcent[18] G.Mirabelli[39] J.Mnich[1] G.B.Mohanty[9] G.S.Muanza[24] A.J.M.Muijs[2] M.Musy[39] S.Nagy[15] S.Natale[20] M.Napolitano[29] F.Nessi-Tedaldi[49] H.Newman[32] A.Nisati[39] T.Novak[31] H.Nowak[48] R.Ofierzynski[49] G.Organtini[39] I.Pal[46] C.Palomares[25] P.Paolucci[29] R.Paramatti[39] G.Passaleva[17] S.Patricelli[29] T.Paul[10] M.Pauluzzi[33] C.Paus[13] F.Pauss[49] M.Pedace[39] S.Pensotti[27] D.Perret-Gallix[4] D.Piccolo[29] F.Pierella[8] M.Pieri[41] M.Pioppi[33] P.A.Piroué[37] E.Pistolesi[27] V.Plyaskin[28] M.Pohl[20] V.Pojidaev[17] J.Pothier[18] D.Prokofiev[34] G.Rahal-Callot[49] M.A.Rahaman[9] P.Raics[15] N.Raja[9] R.Ramelli[49] P.G.Rancoita[27] R.Ranieri[17] A.Raspereza[48] P.Razis[30] S.Rembeczki[26] D.Ren[49] M.Rescigno[39] S.Reucroft[10] S.Riemann[48] K.Riles[3] B.P.Roe[3] L.Romero[25] A.Rosca[48] C.Rosemann[1] C.Rosenbleck[1] S.Rosier-Lees[4] S.Roth[1] J.A.Rubio[18] G.Ruggiero[17] H.Rykaczewski[49] A.Sakharov[49] S.Saremi[6] S.Sarkar[39] J.Salicio[18] E.Sanchez[25] C.Schäfer[18] V.Schegelsky[34] H.Schopper[21] D.J.Schotanus[31] C.Sciacca[29] L.Servoli[33] S.Shevchenko[32] N.Shivarov[42] V.Shoutko[13] E.Shumilov[28] A.Shvorob[32] D.Son[43] C.Souga[24] P.Spillantini[17] M.Steuer[13] D.P.Stickland[37] B.Stoyanov[42] A.Straessner[20] K.Sudhakar[9] G.Sultanov[42] L.Z.Sun[22] S.Sushkov[1] H.Suter[49] J.D.Swain[10] Z.Szillasi[26,¶] X.W.Tang[7] P.Tarjan[15] L.Tauscher[5] L.Taylor[10] B.Tellili[24] D.Teyssier[24] C.Timmermans[31] Samuel C.C.Ting[13] S.M.Ting[13] S.C.Tonwar[9] J.Tóth[12] C.Tully[37] K.L.Tung[7] J.Ulbricht[49] E.Valente[39] R.T.Van de Walle[31] R.Vasquez[46] G.Vesztergombi[12] I.Vetlitsky[28] G.Viertel[49] S.Villa[38] M.Vivargent[4] S.Vlachos[5] I.Vodopianov[26] H.Vogel[35] H.Vogt[48] I.Vorobiev[35,28] A.A.Vorobyov[34] M.Wadhwa[5] Q.Wang[31] X.L.Wang[22] Z.M.Wang[22] M.Weber[18] S.Wynhoff[37,†] L.Xia[32] Z.Z.Xu[22] J.Yamamoto[3] B.Z.Yang[22] C.G.Yang[7] H.J.Yang[3] M.Yang[7] S.C.Yeh[45] An.Zalite[34] Yu.Zalite[34] Z.P.Zhang[22] J.Zhao[22] G.Y.Zhu[7] R.Y.Zhu[32] H.L.Zhuang[7] A.Zichichi[8,18,19] B.Zimmermann[49] M.Zöller[1]

1 III. Physikalisches Institut, RWTH, D-52056 Aachen, Germany[§]
2 National Institute for High Energy Physics, NIKHEF, and University of Amsterdam, NL-1009 DB Amsterdam, The Netherlands
3 University of Michigan, Ann Arbor, MI 48109, USA
4 Laboratoire d'Annecy-le-Vieux de Physique des Particules, LAPP,IN2P3-CNRS, BP 110, F-74941 Annecy-le-Vieux CEDEX, France
5 Institute of Physics, University of Basel, CH-4056 Basel, Switzerland
6 Louisiana State University, Baton Rouge, LA 70803, USA
7 Institute of High Energy Physics, IHEP, 100039 Beijing, China[△]
8 University of Bologna and INFN-Sezione di Bologna, I-40126 Bologna, Italy
9 Tata Institute of Fundamental Research, Mumbai (Bombay) 400 005, India
10 Northeastern University, Boston, MA 02115, USA
11 Institute of Atomic Physics and University of Bucharest, R-76900 Bucharest, Romania
12 Central Research Institute for Physics of the Hungarian Academy of Sciences, H-1525 Budapest 114, Hungary[‡]
13 Massachusetts Institute of Technology, Cambridge, MA 02139, USA
14 Panjab University, Chandigarh 160 014, India
15 KLTE-ATOMKI, H-4010 Debrecen, Hungary[¶]
16 UCD School of Physics, University College Dublin, Belfield, Dublin 4, Ireland
17 INFN Sezione di Firenze and University of Florence, I-50125 Florence, Italy
18 European Laboratory for Particle Physics, CERN, CH-1211 Geneva 23, Switzerland
19 World Laboratory, FBLJA Project, CH-1211 Geneva 23, Switzerland
20 University of Geneva, CH-1211 Geneva 4, Switzerland
21 University of Hamburg, D-22761 Hamburg, Germany
22 Chinese University of Science and Technology, USTC, Hefei, Anhui 230 029, China[△]
23 University of Lausanne, CH-1015 Lausanne, Switzerland
24 Institut de Physique Nucléaire de Lyon, IN2P3-CNRS,Université Claude Bernard, F-69622 Villeurbanne, France
25 Centro de Investigaciones Energéticas, Medioambientales y Tecnológicas, CIEMAT, E-28040 Madrid, Spain[♭]
26 Florida Institute of Technology, Melbourne, FL 32901, USA
27 INFN-Sezione di Milano, I-20133 Milan, Italy
28 Institute of Theoretical and Experimental Physics, ITEP, Moscow, Russia
29 INFN-Sezione di Napoli and University of Naples, I-80125 Naples, Italy
30 Department of Physics, University of Cyprus, Nicosia, Cyprus
31 Radboud University and NIKHEF, NL-6525 ED Nijmegen, The Netherlands
32 California Institute of Technology, Pasadena, CA 91125, USA
33 INFN-Sezione di Perugia and Università Degli Studi di Perugia, I-06100 Perugia, Italy
34 Nuclear Physics Institute, St. Petersburg, Russia
35 Carnegie Mellon University, Pittsburgh, PA 15213, USA
36 INFN-Sezione di Napoli and University of Potenza, I-85100 Potenza, Italy
37 Princeton University, Princeton, NJ 08544, USA
38 University of Californa, Riverside, CA 92521, USA
39 INFN-Sezione di Roma and University of Rome, "La Sapienza", I-00185 Rome, Italy
40 University and INFN, Salerno, I-84100 Salerno, Italy
41 University of California, San Diego, CA 92093, USA
42 Bulgarian Academy of Sciences, Central Lab. of Mechatronics and Instrumentation, BU-1113 Sofia, Bulgaria
43 The Center for High Energy Physics, Kyungpook National University, 702-701 Taegu, Republic of Korea
44 National Central University, Chung-Li, Taiwan, China
45 Department of Physics, National Tsing Hua University, Taiwan, China
46 Purdue University, West Lafayette, IN 47907, USA
47 Paul Scherrer Institut, PSI, CH-5232 Villigen, Switzerland
48 DESY, D-15738 Zeuthen, Germany
49 Eidgenössische Technische Hochschule, ETH Zürich, CH-8093 Zürich, Switzerland

$\langle\sqrt{s}\rangle$ (GeV)	$\mathcal{L}$ (pb^{-1})	Named as
$\mathrm{e^+e^-} \to \mathrm{hadrons}\,(\gamma)$		
191.6	29.8	192 GeV
195.5	83.7	196 GeV
199.6	83.2	200 GeV
201.8	36.8	202 GeV
204.9	75.9	205 GeV
206.5	130.5	207 GeV
208.0	8.3	208 GeV
$\mathrm{e^+e^-} \to \mu^+\mu^-(\gamma)$		
191.6	28.0	192 GeV
195.5	82.1	196 GeV
199.6	80.4	200 GeV
201.9	38.1	202 GeV
205.0	73.5	205 GeV
206.5	126.8	207 GeV
208.0	8.1	208 GeV
$\mathrm{e^+e^-} \to \tau^+\tau^-(\gamma)$		
191.6	28.9	192 GeV
195.5	81.7	196 GeV
199.5	72.3	200 GeV
201.7	38.1	202 GeV
205.2	73.5	205 GeV
206.7	125.9	207 GeV
208.1	8.1	208 GeV
$\mathrm{e^+e^-} \to \mathrm{e^+e^-}(\gamma)$		
191.6	27.5	192 GeV
195.5	82.7	196 GeV
199.5	82.6	200 GeV
201.8	37.0	202 GeV
205.2	66.9	205 GeV
206.7	122.7	207 GeV
208.2	7.9	208 GeV

Table 2: Average centre-of-mass energies and corresponding integrated luminosities of the data samples, together with the names used in the following Tables. Luminosity differences across the channels are due to different data-quality requirements, which also result in slightly different average values.

$\sqrt{s}$ (GeV)	192	196	200	202	205	207	208
$e^+e^- \to$ hadrons (γ)							
Selection Efficiency	89.1 ± 0.1	88.9 ± 0.1	87.5 ± 0.1	88.5 ± 0.2	87.6 ± 0.1	87.5 ± 0.0	87.4 ± 0.1
Total Background	9.8	10.7	11.1	11.3	11.8	12.2	13.4
$e^+e^- \to e^+e^-$ hadrons	2.9	3.1	3.1	3.0	3.3	3.4	3.7
$e^+e^- \to W^+W^-$	5.2	5.7	6.0	6.3	6.4	6.6	7.3
Other	1.5	1.7	1.8	1.8	1.9	2.0	2.2
ISR Contamination	0.2	0.2	0.2	0.2	0.2	0.2	0.2
$e^+e^- \to \mu^+\mu^- (\gamma)$							
Selection Efficiency	60.8 ± 0.8	59.1 ± 0.8	59.0 ± 0.8	59.5 ± 0.8	61.1 ± 0.6	62.1 ± 0.6	61.5 ± 0.8
Total Background	16.6 ± 1.4	18.6 ± 1.5	17.1 ± 1.7	21.0 ± 1.8	19.5 ± 1.1	24.6 ± 1.2	18.9 ± 1.1
$e^+e^- \to e^+e^-\ell^+\ell^-$	9.8 ± 1.3	11.1 ± 1.4	10.0 ± 1.6	13.3 ± 1.6	11.7 ± 0.9	15.3 ± 1.1	12.2 ± 0.9
$e^+e^- \to W^+W^-$	3.4 ± 0.2	3.4 ± 0.2	3.5 ± 0.2	3.3 ± 0.2	3.4 ± 0.4	4.0 ± 0.4	3.5 ± 0.3
Cosmic Rays	0.5 ± 0.3	0.3 ± 0.1	0.2 ± 0.1	0.2 ± 0.2	0.8 ± 0.2	1.0 ± 0.2	0.5 ± 0.5
Other	2.5 ± 0.3	3.5 ± 0.3	3.0 ± 0.2	3.9 ± 0.7	3.2 ± 0.2	4.2 ± 0.2	2.5 ± 0.2
ISR Contamination	0.4 ± 0.1	0.3 ± 0.1	0.4 ± 0.1	0.3 ± 0.1	0.4 ± 0.1	0.1 ± 0.1	0.2 ± 0.1
$e^+e^- \to \tau^+\tau^- (\gamma)$							
Selection Efficiency	44.0 ± 0.5	43.9 ± 0.5	43.3 ± 0.6	42.9 ± 0.5	40.9 ± 0.5	41.8 ± 0.5	41.0 ± 0.7
Total Background	21.0 ± 1.6	23.1 ± 0.9	22.5 ± 1.4	21.9 ± 1.8	24.8 ± 1.3	26.1 ± 1.8	23.7 ± 2.7
$e^+e^- \to e^+e^-\ell^+\ell^-$	10.4 ± 1.1	11.4 ± 0.6	11.3 ± 1.2	10.2 ± 1.5	13.9 ± 0.9	14.2 ± 1.3	12.6 ± 1.2
Other	10.1 ± 1.1	11.3 ± 0.7	10.7 ± 0.7	11.5 ± 1.0	10.5 ± 0.9	11.4 ± 1.2	10.7 ± 2.4
ISR Contamination	0.5 ± 0.1	0.4 ± 0.1	0.5 ± 0.1	0.2 ± 0.1	0.4 ± 0.1	0.5 ± 0.1	0.4 ± 0.1
$e^+e^- \to e^+e^- (\gamma)$							
Selection Efficiency	96.7 ± 0.2	97.2 ± 0.2	95.7 ± 0.3	97.0 ± 0.2	96.8 ± 0.2	97.5 ± 0.2	96.9 ± 0.4
Total Background	4.4 ± 0.2	4.1 ± 0.2	4.4 ± 0.2	4.4 ± 0.2	4.3 ± 0.2	4.3 ± 0.2	4.4 ± 0.3
$e^+e^- \to \tau^+\tau^-$	2.9 ± 0.2	2.7 ± 0.2	2.9 ± 0.2	3.0 ± 0.2	2.9 ± 0.2	2.9 ± 0.2	3.1 ± 0.3
$e^+e^- \to W^+W^-$	0.7 ± 0.1	0.5 ± 0.1	0.5 ± 0.1	0.5 ± 0.1	0.4 ± 0.1	0.4 ± 0.1	0.3 ± 0.1
Other	0.8 ± 0.1	0.9 ± 0.1	1.0 ± 0.1	0.9 ± 0.2	1.0 ± 0.1	1.0 ± 0.1	1.0 ± 0.1

Table 3: Selection efficiencies, background fractions and their breakdown, all in %, for the inclusive samples. The uncertainties reflect the limited Monte Carlo statistics and are negligible for the background to the $e^+e^- \to$ hadrons (γ) channel. Values for the $e^+e^- \to e^+e^- (\gamma)$ channel refer to the angular region $|\cos\theta| < 0.72$.

$\sqrt{s}$ (GeV)	192	196	200	202	205	207	208
$e^+e^- \to$ hadrons (γ)							
Selection Efficiency	85.7 ± 0.3	85.5 ± 0.2	84.7 ± 0.3	85.8 ± 0.3	85.2 ± 0.1	85.2 ± 0.1	85.0 ± 0.1
Total Background	15.7 ± 0.3	17.2 ± 0.2	17.5 ± 0.3	17.0 ± 0.3	17.9 ± 0.1	18.4 ± 0.1	20.8 ± 0.1
$e^+e^- \to e^+e^-$ hadrons	0.2	0.1	0.2	0.1	0.1	0.2	0.2
$e^+e^- \to W^+W^-$	7.5	8.4	9.0	9.1	9.6	9.8	11.3
Other	0.8	0.9	1.1	0.9	1.0	1.0	1.2
ISR Contamination	7.2 ± 0.3	7.8 ± 0.2	7.3 ± 0.2	6.9 ± 0.2	7.2 ± 0.1	7.4 ± 0.1	8.1 ± 0.1
$e^+e^- \to \mu^+\mu^- (\gamma)$							
Selection Efficiency	71.1 ± 1.1	71.1 ± 1.1	70.5 ± 1.1	74.0 ± 1.0	76.1 ± 0.7	76.4 ± 0.7	77.7 ± 0.9
Total Background	16.1 ± 5.9	13.2 ± 3.9	11.7 ± 3.9	15.4 ± 4.3	14.5 ± 4.0	15.8 ± 4.0	17.1 ± 4.5
$e^+e^- \to e^+e^-\ell^+\ell^-$	5.7 ± 1.8	5.0 ± 1.5	3.4 ± 1.5	6.0 ± 1.7	5.3 ± 1.1	5.6 ± 1.1	5.7 ± 1.1
$e^+e^- \to W^+W^-$	2.6 ± 0.2	2.8 ± 0.2	3.0 ± 0.3	2.7 ± 0.2	3.0 ± 0.5	3.9 ± 0.6	4.4 ± 0.5
Cosmic	0.7 ± 0.5	0.2 ± 0.1	0.3 ± 0.2	0.2 ± 0.2	0.4 ± 0.2	0.6 ± 0.2	1.2 ± 1.2
Other	1.5 ± 0.2	1.6 ± 0.2	1.5 ± 0.2	2.6 ± 1.2	2.0 ± 0.2	1.9 ± 0.2	1.5 ± 0.2
ISR Contamination	5.6 ± 0.7	3.6 ± 0.5	3.5 ± 0.5	3.9 ± 0.5	3.8 ± 0.2	3.8 ± 0.3	4.3 ± 0.5
$e^+e^- \to \tau^+\tau^- (\gamma)$							
Selection Efficiency	51.5 ± 0.8	51.7 ± 0.8	52.1 ± 0.8	50.6 ± 0.8	48.3 ± 0.8	51.0 ± 0.8	46.7 ± 1.1
Total Background	15.8 ± 2.1	15.1 ± 1.4	14.1 ± 1.5	14.8 ± 1.9	16.4 ± 1.7	20.5 ± 2.5	22.9 ± 5.7
$e^+e^- \to e^+e^-\ell^+\ell^-$	2.2 ± 0.7	1.8 ± 0.3	2.2 ± 0.6	1.1 ± 0.6	2.3 ± 0.5	3.0 ± 0.9	2.8 ± 0.9
Other	10.4 ± 1.8	9.9 ± 1.1	9.3 ± 1.1	10.6 ± 1.6	10.8 ± 1.4	13.8 ± 2.2	15.9 ± 5.4
ISR Contamination	3.2 ± 0.9	3.4 ± 0.8	2.6 ± 0.8	3.1 ± 0.8	3.3 ± 0.8	3.7 ± 0.9	4.2 ± 1.4
$e^+e^- \to e^+e^- (\gamma)$							
Selection Efficiency	97.3 ± 0.2	97.7 ± 0.2	96.4 ± 0.3	97.6 ± 0.2	97.5 ± 0.2	98.0 ± 0.2	97.7 ± 0.3
Total Background	3.9 ± 0.3	3.4 ± 0.2	3.8 ± 0.3	3.8 ± 0.3	3.7 ± 0.2	3.8 ± 0.3	3.7 ± 0.4
$e^+e^- \to \tau^+\tau^-$	2.8 ± 0.2	2.6 ± 0.2	2.9 ± 0.2	3.0 ± 0.2	2.9 ± 0.2	2.9 ± 0.2	3.0 ± 0.3
$e^+e^- \to W^+W^-$	0.8 ± 0.1	0.5 ± 0.1	0.6 ± 0.1	0.5 ± 0.1	0.4 ± 0.1	0.5 ± 0.1	0.3 ± 0.1
Other	0.3 ± 0.1	0.3 ± 0.1	0.3 ± 0.1	0.3 ± 0.1	0.4 ± 0.1	0.4 ± 0.1	0.4 ± 0.1

Table 4: Selection efficiencies, background fractions and their breakdown, all in %, for the high-energy samples. The uncertainties reflect the limited Monte Carlo statistics and are negligible for the background to the $e^+e^- \to$ hadrons (γ) channel. Values for the $e^+e^- \to e^+e^- (\gamma)$ channel refer to the angular region $|\cos\theta| < 0.72$.

	Inclusive sample			High-energy sample		
$\sqrt{s}$ (GeV)	N_{sel}	σ (pb)	σ_{SM} (pb)	N_{sel}	σ (pb)	σ_{SM} (pb)
$\mathrm{e^+e^-} \rightarrow \mathrm{hadrons}(\gamma)$						
192	2767	$93.76 \pm 1.98 \pm 0.99$	92.91	679	$22.38 \pm 1.02 \pm 0.19$	21.32
196	7166	$86.05 \pm 1.14 \pm 0.93$	88.17	1740	$20.14 \pm 0.58 \pm 0.16$	20.21
200	6753	$82.45 \pm 1.13 \pm 0.88$	83.61	1629	$19.09 \pm 0.57 \pm 0.16$	19.13
202	2956	$80.51 \pm 1.67 \pm 0.87$	81.32	736	$19.33 \pm 0.89 \pm 0.16$	18.59
205	5949	$78.95 \pm 1.16 \pm 0.82$	78.27	1452	$18.46 \pm 0.59 \pm 0.14$	17.87
207	9888	$76.07 \pm 0.87 \pm 0.82$	76.77	2430	$17.87 \pm 0.44 \pm 0.13$	17.52
208	578	$68.78 \pm 3.30 \pm 0.83$	75.40	135	$15.09 \pm 1.64 \pm 0.14$	17.20
$\mathrm{e^+e^-} \rightarrow \mu^+\mu^-(\gamma)$						
192	131	$6.41 \pm 0.67 \pm 0.21$	7.02	61	$2.54 \pm 0.39 \pm 0.09$	3.11
196	397	$6.52 \pm 0.41 \pm 0.25$	6.67	207	$3.05 \pm 0.25 \pm 0.10$	2.97
200	349	$6.09 \pm 0.39 \pm 0.23$	6.37	185	$2.85 \pm 0.24 \pm 0.09$	2.84
202	175	$6.08 \pm 0.58 \pm 0.24$	6.20	99	$2.97 \pm 0.35 \pm 0.10$	2.76
205	358	$6.53 \pm 0.43 \pm 0.32$	5.95	157	$2.37 \pm 0.22 \pm 0.07$	2.67
207	521	$5.05 \pm 0.29 \pm 0.17$	5.88	260	$2.24 \pm 0.17 \pm 0.06$	2.63
208	44	$7.70 \pm 1.44 \pm 0.28$	5.79	17	$2.49 \pm 0.74 \pm 0.10$	2.59
$\mathrm{e^+e^-} \rightarrow \tau^+\tau^-(\gamma)$						
192	116	$7.21 \pm 0.85 \pm 0.20$	7.01	52	$2.93 \pm 0.48 \pm 0.06$	3.11
196	300	$6.42 \pm 0.48 \pm 0.24$	6.68	161	$3.22 \pm 0.30 \pm 0.07$	2.97
200	263	$6.52 \pm 0.52 \pm 0.23$	6.37	131	$2.97 \pm 0.30 \pm 0.07$	2.84
202	123	$5.86 \pm 0.68 \pm 0.22$	6.20	64	$2.81 \pm 0.42 \pm 0.07$	2.77
205	261	$6.51 \pm 0.54 \pm 0.28$	5.98	125	$2.93 \pm 0.32 \pm 0.07$	2.68
207	406	$5.70 \pm 0.38 \pm 0.23$	5.88	189	$2.34 \pm 0.21 \pm 0.08$	2.63
208	29	$6.65 \pm 1.62 \pm 0.27$	5.78	11	$2.23 \pm 0.88 \pm 0.07$	2.59
$\mathrm{e^+e^-} \rightarrow \mathrm{e^+e^-}(\gamma)$						
192	659	$23.71 \pm 0.92 \pm 0.32$	24.00	624	$22.46 \pm 0.90 \pm 0.11$	22.68
196	1899	$22.65 \pm 0.52 \pm 0.31$	23.04	1781	$21.27 \pm 0.50 \pm 0.11$	21.76
200	1776	$21.49 \pm 0.51 \pm 0.29$	21.98	1668	$20.14 \pm 0.49 \pm 0.10$	20.86
202	857	$22.82 \pm 0.78 \pm 0.31$	21.45	811	$21.62 \pm 0.76 \pm 0.11$	20.36
205	1483	$21.94 \pm 0.57 \pm 0.30$	20.91	1380	$20.39 \pm 0.55 \pm 0.10$	19.75
207	2572	$20.60 \pm 0.41 \pm 0.28$	20.41	2418	$19.36 \pm 0.39 \pm 0.10$	19.47
208	144	$18.00 \pm 1.50 \pm 0.25$	20.06	137	$17.10 \pm 1.46 \pm 0.09$	19.16

Table 5: Numbers of selected events, N_{sel}, measured cross sections, σ, with their statistical and systematic uncertainties and corresponding Standard Model predictions for the inclusive and high-energy samples. Results for the $\mathrm{e^+e^-} \rightarrow \mathrm{e^+e^-}(\gamma)$ process refer to the range $|\cos\theta| < 0.72$. The theoretical uncertainties on the Standard Model predictions are estimated to be below 1% except for large-angle Bhabha scattering where they reach 1.5% [32].

$\sqrt{s}$ (GeV)	Inclusive sample				High-energy sample			
	N_{f}	N_{b}	A_{fb}	$A_{\mathrm{fb}}^{\mathrm{SM}}$	N_{f}	N_{b}	A_{fb}	$A_{\mathrm{fb}}^{\mathrm{SM}}$
$\mathrm{e}^{+}\mathrm{e}^{-} \rightarrow \mu^{+}\mu^{-}(\gamma)$								
192	82	49	$0.43 \pm 0.13 \pm 0.09$	0.308	48	13	$0.69 \pm 0.12 \pm 0.07$	0.569
196	259	129	$0.33 \pm 0.07 \pm 0.04$	0.306	151	46	$0.53 \pm 0.07 \pm 0.04$	0.564
200	226	123	$0.31 \pm 0.07 \pm 0.04$	0.304	126	59	$0.44 \pm 0.08 \pm 0.04$	0.560
202	121	54	$0.36 \pm 0.10 \pm 0.05$	0.303	75	24	$0.59 \pm 0.09 \pm 0.02$	0.557
205	236	122	$0.34 \pm 0.07 \pm 0.05$	0.302	110	47	$0.48 \pm 0.09 \pm 0.03$	0.554
207	346	175	$0.32 \pm 0.06 \pm 0.03$	0.302	189	71	$0.54 \pm 0.06 \pm 0.02$	0.553
208	33	11	$0.36 \pm 0.20 \pm 0.10$	0.301	14	3	$0.72 \pm 0.16 \pm 0.04$	0.551
$\mathrm{e}^{+}\mathrm{e}^{-} \rightarrow \tau^{+}\tau^{-}(\gamma)$								
192	54	27	$0.38 \pm 0.13 \pm 0.04$	0.311	35	8	$0.52 \pm 0.12 \pm 0.05$	0.569
196	142	80	$0.33 \pm 0.08 \pm 0.03$	0.309	95	34	$0.44 \pm 0.09 \pm 0.05$	0.565
200	110	74	$0.18 \pm 0.10 \pm 0.03$	0.307	66	28	$0.46 \pm 0.10 \pm 0.05$	0.560
202	60	27	$0.34 \pm 0.13 \pm 0.05$	0.305	37	8	$0.47 \pm 0.13 \pm 0.08$	0.557
205	123	57	$0.44 \pm 0.10 \pm 0.04$	0.303	77	20	$0.56 \pm 0.09 \pm 0.05$	0.554
207	204	88	$0.35 \pm 0.07 \pm 0.04$	0.302	110	20	$0.61 \pm 0.07 \pm 0.09$	0.553
208	10	10	$0.00 \pm 0.30 \pm 0.05$	0.301	6	3	$0.08 \pm 0.35 \pm 0.09$	0.551
$\mathrm{e}^{+}\mathrm{e}^{-} \rightarrow \mathrm{e}^{+}\mathrm{e}^{-}(\gamma)$								
192	405	59	$0.839 \pm 0.027 \pm 0.010$	0.782	395	53	$0.863 \pm 0.025 \pm 0.007$	0.815
196	1121	203	$0.778 \pm 0.018 \pm 0.010$	0.785	1096	191	$0.796 \pm 0.018 \pm 0.007$	0.815
200	1048	174	$0.801 \pm 0.018 \pm 0.010$	0.787	1047	168	$0.814 \pm 0.018 \pm 0.007$	0.816
202	480	94	$0.759 \pm 0.029 \pm 0.010$	0.789	468	84	$0.791 \pm 0.028 \pm 0.007$	0.816
205	820	145	$0.777 \pm 0.022 \pm 0.010$	0.791	799	132	$0.803 \pm 0.021 \pm 0.007$	0.817
207	1430	242	$0.791 \pm 0.016 \pm 0.010$	0.792	1393	228	$0.805 \pm 0.016 \pm 0.007$	0.817
208	81	16	$0.719 \pm 0.076 \pm 0.010$	0.793	79	14	$0.750 \pm 0.073 \pm 0.007$	0.818

Table 6: Measurements of the forward-backward asymmetries of lepton-pair production, A_{fb}, with statistical and systematic uncertainties. The corresponding Standard Model predictions, $A_{\mathrm{fb}}^{\mathrm{SM}}$, are also given, together with the numbers of events selected in the forward, N_{f}, and backward, N_{b}, hemispheres. Results for the $\mathrm{e}^{+}\mathrm{e}^{-} \rightarrow \mathrm{e}^{+}\mathrm{e}^{-}(\gamma)$ process refer to $|\cos\theta| < 0.72$.

$|\cos\theta^\star|$	N_{data}	f_{back} (%)	ε (%)	$\frac{\mathrm{d}\sigma}{\mathrm{d}|\cos\theta^\star|}$ (pb)	$\frac{\mathrm{d}\sigma}{\mathrm{d}|\cos\theta^\star|}\big|_{\text{SM}}$ (pb)
			$\sqrt{s} = 192$ GeV		
$0.00 - 0.09$	24	6.7 ± 4.9	97.6 ± 1.4	$9.3 \pm\ \ 1.9 \pm\ \ 0.2$	10.1
$0.09 - 0.18$	26	6.8 ± 4.8	96.4 ± 1.6	$10.2 \pm\ \ 2.0 \pm\ \ 0.2$	11.0
$0.18 - 0.27$	30	6.2 ± 4.0	99.4 ± 0.6	$11.5 \pm\ \ 2.1 \pm\ \ 0.1$	13.0
$0.27 - 0.36$	37	6.5 ± 3.9	97.9 ± 1.1	$14.3 \pm\ \ 2.4 \pm\ \ 0.2$	16.6
$0.36 - 0.45$	60	4.8 ± 2.7	98.0 ± 0.8	$23.6 \pm\ \ 3.0 \pm\ \ 0.3$	22.9
$0.45 - 0.54$	78	3.7 ± 2.0	98.4 ± 0.6	$30.9 \pm\ \ 3.5 \pm\ \ 0.2$	34.2
$0.54 - 0.63$	151	2.4 ± 1.3	97.6 ± 0.6	$61.1 \pm\ \ 5.0 \pm\ \ 0.4$	55.9
$0.63 - 0.72$	220	1.3 ± 0.8	80.3 ± 1.1	$109.4 \pm\ \ 7.4 \pm\ \ 1.7$	102.6
$0.72 - 0.81$	25	3.1 ± 3.3	5.0 ± 0.4	$196.4 \pm 39.3 \pm 16.2$	225.1
$0.81 - 0.90$	1325	2.0 ± 0.4	73.0 ± 0.5	$720.4 \pm 19.8 \pm\ \ 6.0$	713.5
			$\sqrt{s} = 196$ GeV		
$0.00 - 0.09$	69	8.0 ± 3.0	99.1 ± 0.6	$8.6 \pm\ \ 1.0 \pm\ \ 0.1$	9.6
$0.09 - 0.18$	82	7.4 ± 2.7	97.1 ± 1.1	$10.5 \pm\ \ 1.2 \pm\ \ 0.2$	10.5
$0.18 - 0.27$	94	6.2 ± 2.5	98.9 ± 0.6	$12.0 \pm\ \ 1.2 \pm\ \ 0.1$	12.4
$0.27 - 0.36$	138	5.0 ± 2.0	97.7 ± 0.8	$18.0 \pm\ \ 1.5 \pm\ \ 0.2$	15.9
$0.36 - 0.45$	159	4.6 ± 1.6	98.7 ± 0.5	$20.6 \pm\ \ 1.6 \pm\ \ 0.2$	21.9
$0.45 - 0.54$	247	3.4 ± 1.1	99.0 ± 0.4	$32.4 \pm\ \ 2.1 \pm\ \ 0.1$	32.8
$0.54 - 0.63$	380	2.3 ± 0.8	97.4 ± 0.5	$51.2 \pm\ \ 2.6 \pm\ \ 0.3$	53.6
$0.63 - 0.72$	616	1.0 ± 0.4	82.5 ± 0.8	$99.3 \pm\ \ 4.0 \pm\ \ 1.2$	98.5
$0.72 - 0.81$	80	3.0 ± 1.9	4.9 ± 0.3	$211.2 \pm 23.6 \pm 13.9$	216.2
$0.81 - 0.90$	3812	2.0 ± 0.2	72.7 ± 0.4	$690.4 \pm 11.2 \pm\ \ 5.0$	685.1
			$\sqrt{s} = 200$ GeV		
$0.00 - 0.09$	83	11.1 ± 3.7	96.3 ± 1.3	$10.3 \pm\ \ 1.1 \pm\ \ 0.2$	9.2
$0.09 - 0.18$	78	9.7 ± 3.4	96.8 ± 1.2	$9.8 \pm\ \ 1.1 \pm\ \ 0.2$	10.0
$0.18 - 0.27$	93	5.2 ± 2.3	97.0 ± 1.0	$12.2 \pm\ \ 1.3 \pm\ \ 0.2$	11.9
$0.27 - 0.36$	111	5.7 ± 2.2	95.7 ± 1.0	$14.7 \pm\ \ 1.4 \pm\ \ 0.2$	15.2
$0.36 - 0.45$	154	4.9 ± 1.7	98.2 ± 0.6	$20.0 \pm\ \ 1.6 \pm\ \ 0.2$	21.0
$0.45 - 0.54$	211	3.8 ± 1.2	97.3 ± 0.6	$28.0 \pm\ \ 1.9 \pm\ \ 0.2$	31.5
$0.54 - 0.63$	355	2.1 ± 0.7	94.6 ± 0.6	$49.4 \pm\ \ 2.6 \pm\ \ 0.3$	51.5
$0.63 - 0.72$	588	1.0 ± 0.4	79.2 ± 0.8	$98.9 \pm\ \ 4.1 \pm\ \ 1.3$	94.6
$0.72 - 0.81$	74	5.8 ± 2.9	4.1 ± 0.3	$231.3 \pm 26.9 \pm 16.1$	207.7
$0.81 - 0.90$	3635	2.1 ± 0.2	71.4 ± 0.4	$670.3 \pm 11.1 \pm\ \ 4.9$	658.4

Table 7: Differential cross section for the $e^+e^- \to e^+e^-(\gamma)$ process, $\mathrm{d}\sigma/\mathrm{d}|\cos\theta^\star|$, as a function of the absolute value of the scattering angle, $|\cos\theta^\star|$. The first uncertainty is statistical and the second systematic. The numbers of observed events, N_{data}, and the background fractions, f_{back}, are also given, together with the selection efficiency, ε. Both f_{back} and ε are in %. The Standard Model predictions, as computed with the BHWIDE Monte Carlo program, are also given. Only high-energy events with $\zeta < 25°$ are considered.

$\lvert \cos\theta^\star \rvert$	N_{data}	f_{back} (%)	ε (%)	$\frac{\mathrm{d}\sigma}{\mathrm{d}\lvert\cos\theta^\star\rvert}$ (pb)	$\frac{\mathrm{d}\sigma}{\mathrm{d}\lvert\cos\theta^\star\rvert}\big\rvert_{\mathrm{SM}}$ (pb)
$\sqrt{s} = 202$ GeV					
$0.00 - 0.09$	40	8.6 ± 4.7	100.0 ± 0.0	$11.0 \pm \quad 1.7 \pm \quad 0.1$	9.0
$0.09 - 0.18$	40	8.7 ± 4.9	99.4 ± 0.6	$11.0 \pm \quad 1.7 \pm \quad 0.2$	9.8
$0.18 - 0.27$	42	6.3 ± 3.8	99.0 ± 0.7	$11.9 \pm \quad 1.8 \pm \quad 0.1$	11.6
$0.27 - 0.36$	51	6.1 ± 3.3	97.1 ± 1.0	$14.8 \pm \quad 2.1 \pm \quad 0.2$	14.9
$0.36 - 0.45$	73	4.6 ± 2.5	98.6 ± 0.6	$21.2 \pm \quad 2.5 \pm \quad 0.2$	20.6
$0.45 - 0.54$	126	3.7 ± 1.8	98.0 ± 0.6	$37.2 \pm \quad 3.3 \pm \quad 0.2$	30.9
$0.54 - 0.63$	185	2.2 ± 1.1	98.0 ± 0.5	$55.4 \pm \quad 4.1 \pm \quad 0.3$	50.5
$0.63 - 0.72$	255	1.1 ± 0.6	82.9 ± 0.9	$91.4 \pm \quad 5.7 \pm \quad 1.2$	92.7
$0.72 - 0.81$	39	3.4 ± 3.2	4.6 ± 0.4	$243.7 \pm 39.0 \pm 18.5$	203.7
$0.81 - 0.90$	1528	2.2 ± 0.4	72.7 ± 0.4	$618.3 \pm 15.8 \pm \quad 4.8$	645.7
$\sqrt{s} = 205$ GeV					
$0.00 - 0.09$	54	6.5 ± 3.2	96.3 ± 1.1	$8.7 \pm \quad 1.2 \pm \quad 0.1$	8.8
$0.09 - 0.18$	84	9.3 ± 3.8	98.0 ± 0.9	$12.9 \pm \quad 1.4 \pm \quad 0.3$	9.6
$0.18 - 0.27$	78	5.8 ± 2.7	99.1 ± 0.5	$12.3 \pm \quad 1.4 \pm \quad 0.1$	11.4
$0.27 - 0.36$	103	6.9 ± 2.6	98.7 ± 0.6	$16.1 \pm \quad 1.6 \pm \quad 0.1$	14.6
$0.36 - 0.45$	124	4.1 ± 1.8	99.0 ± 0.4	$20.0 \pm \quad 1.8 \pm \quad 0.2$	20.2
$0.45 - 0.54$	193	3.5 ± 1.4	97.5 ± 0.6	$31.7 \pm \quad 2.3 \pm \quad 0.2$	30.2
$0.54 - 0.63$	286	2.5 ± 0.9	96.6 ± 0.5	$48.0 \pm \quad 2.8 \pm \quad 0.3$	49.5
$0.63 - 0.72$	462	1.3 ± 0.5	81.2 ± 0.8	$93.3 \pm \quad 4.3 \pm \quad 1.1$	90.9
$0.72 - 0.81$	74	2.6 ± 2.1	4.7 ± 0.3	$252.2 \pm 29.3 \pm 15.3$	199.7
$0.81 - 0.90$	2801	2.0 ± 0.3	72.5 ± 0.3	$628.7 \pm 11.9 \pm \quad 4.4$	633.3
$\sqrt{s} = 207$ GeV					
$0.00 - 0.09$	107	8.0 ± 2.9	99.1 ± 0.9	$9.0 \pm \quad 0.9 \pm \quad 0.1$	8.6
$0.09 - 0.18$	105	9.6 ± 3.0	98.3 ± 1.2	$8.7 \pm \quad 0.9 \pm \quad 0.2$	9.4
$0.18 - 0.27$	120	6.4 ± 2.1	97.5 ± 1.2	$10.4 \pm \quad 1.0 \pm \quad 0.2$	11.2
$0.27 - 0.36$	194	6.1 ± 1.7	98.3 ± 0.9	$16.8 \pm \quad 1.2 \pm \quad 0.2$	14.3
$0.36 - 0.45$	261	4.4 ± 1.4	97.8 ± 0.9	$23.1 \pm \quad 1.4 \pm \quad 0.3$	19.8
$0.45 - 0.54$	330	3.6 ± 1.0	98.0 ± 0.7	$29.4 \pm \quad 1.6 \pm \quad 0.2$	29.7
$0.54 - 0.63$	495	2.5 ± 0.7	98.3 ± 0.5	$44.5 \pm \quad 2.0 \pm \quad 0.2$	48.5
$0.63 - 0.72$	812	1.2 ± 0.4	80.8 ± 1.1	$90.0 \pm \quad 3.2 \pm \quad 1.4$	89.2
$0.72 - 0.81$	94	1.9 ± 1.3	4.9 ± 0.4	$170.0 \pm 17.5 \pm 14.4$	195.9
$0.81 - 0.90$	4871	1.8 ± 0.2	72.1 ± 0.5	$604.4 \pm \quad 8.7 \pm \quad 5.1$	621.2
$\sqrt{s} = 208$ GeV					
$0.00 - 0.09$	3	8.0 ± 11.3	99.1 ± 0.9	$3.9 \pm \quad 2.3 \pm \quad 0.1$	8.5
$0.09 - 0.18$	8	9.6 ± 11.6	98.3 ± 1.2	$10.4 \pm \quad 3.7 \pm \quad 0.2$	9.2
$0.18 - 0.27$	4	6.3 ± 8.4	97.5 ± 1.2	$5.4 \pm \quad 2.7 \pm \quad 0.1$	10.9
$0.27 - 0.36$	10	6.1 ± 6.9	98.3 ± 0.9	$13.4 \pm \quad 4.2 \pm \quad 0.1$	14.0
$0.36 - 0.45$	17	4.4 ± 5.5	97.8 ± 0.9	$23.4 \pm \quad 5.7 \pm \quad 0.3$	19.4
$0.45 - 0.54$	19	3.6 ± 4.1	98.0 ± 0.7	$26.3 \pm \quad 6.0 \pm \quad 0.2$	29.1
$0.54 - 0.63$	27	2.5 ± 2.7	98.3 ± 0.5	$37.6 \pm \quad 7.2 \pm \quad 0.2$	47.6
$0.63 - 0.72$	49	1.2 ± 1.5	80.8 ± 1.1	$84.3 \pm 12.0 \pm \quad 1.3$	87.5
$0.72 - 0.81$	10	1.9 ± 5.2	4.9 ± 0.4	$280.3 \pm 88.7 \pm 23.8$	192.2
$0.81 - 0.90$	294	1.9 ± 0.8	72.1 ± 0.5	$564.8 \pm 32.9 \pm \quad 4.8$	609.5

Table 8: Differential cross section for the $e^+e^- \to e^+e^-(\gamma)$ process, continued from Table 7

24
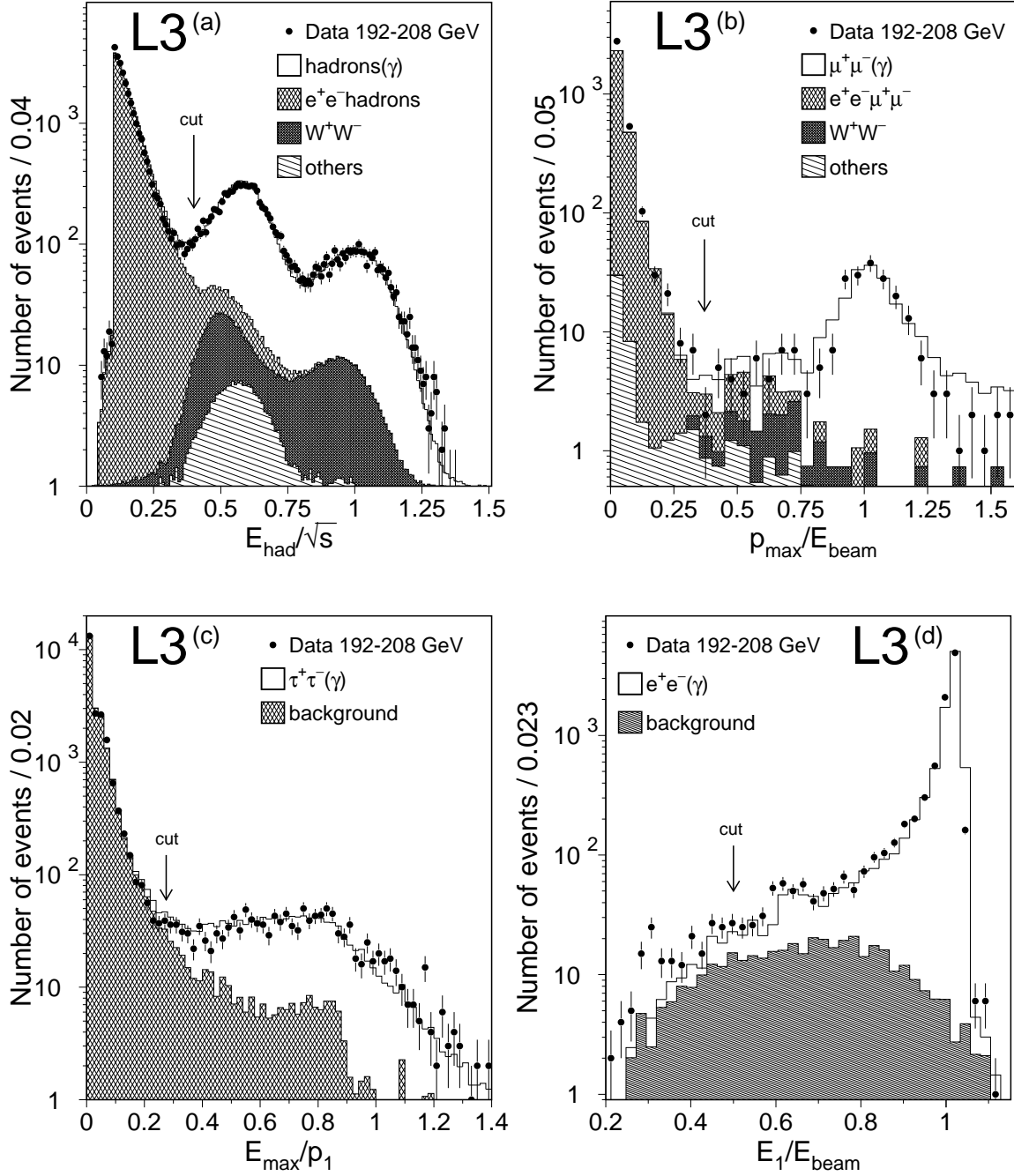
Figure 1: Distributions for data and Monte Carlo of a) the hadronic energy normalised to the centre-of-mass energy for the $e^+e^- \to$ hadrons(γ) analysis, b) the highest muon momentum normalised to the beam energy for the $e^+e^- \to \mu^+\mu^-(\gamma)$ analysis, c) the highest tau-jet energy normalised to the corresponding estimated momentum for the $e^+e^- \to \tau^+\tau^-(\gamma)$ analysis and d) the highest electron energy normalised to the beam energy for the $e^+e^- \to e^+e^-(\gamma)$ analysis. The arrows indicate the positions of the selection cuts. All other cuts are applied.
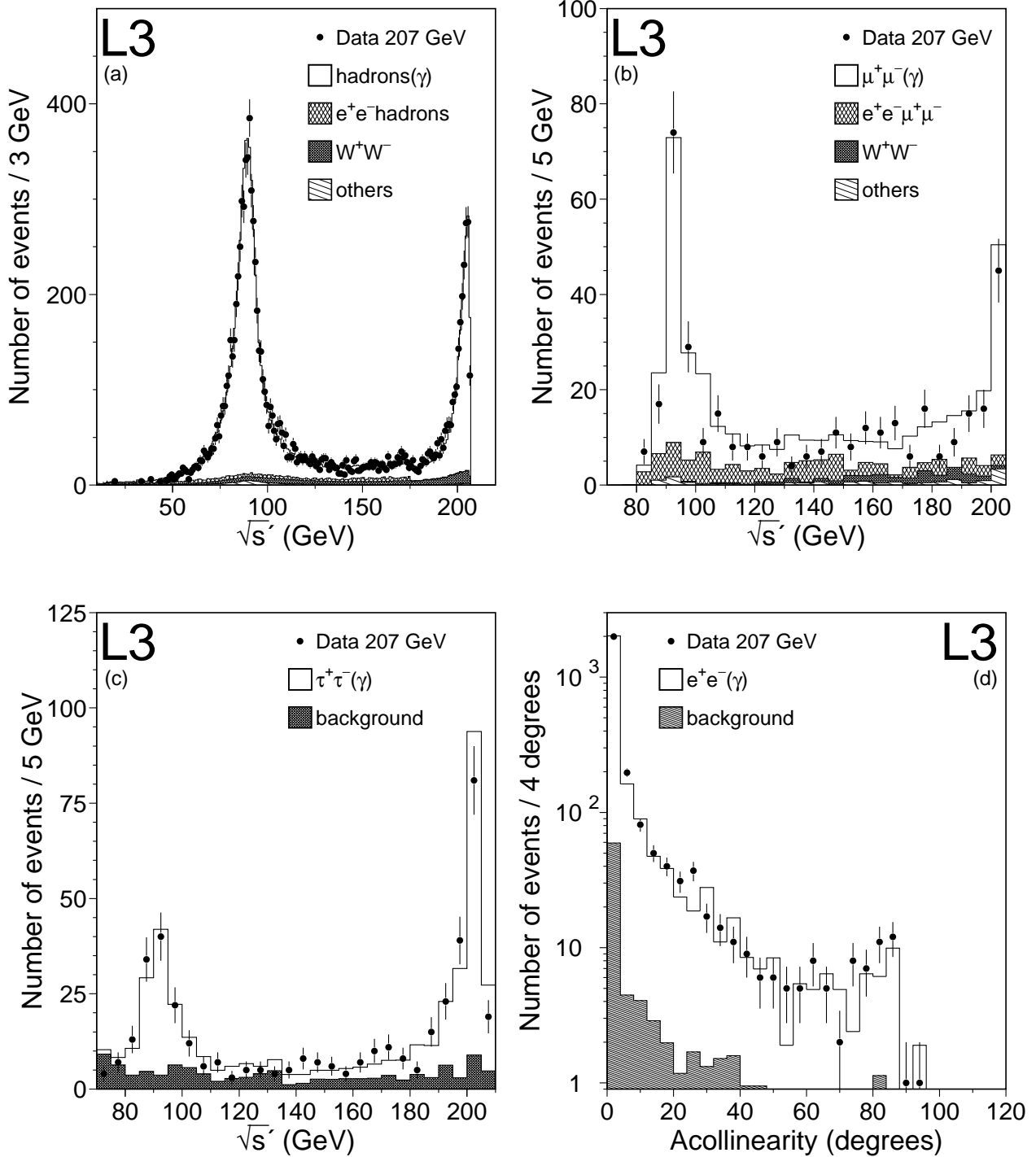
Figure 2: Distributions for data and Monte Carlo at $\sqrt{s} = 207$ GeV of the reconstructed effective centre-of-mass energy, $\sqrt{s'}$, for the a) $e^+e^- \rightarrow$ hadrons (γ), b) $e^+e^- \rightarrow \mu^+\mu^-(\gamma)$ and c) $e^+e^- \rightarrow \tau^+\tau^-(\gamma)$ channels and d) of the reconstructed acollinearity angle, ζ, for the $e^+e^- \rightarrow e^+e^-(\gamma)$ channel.
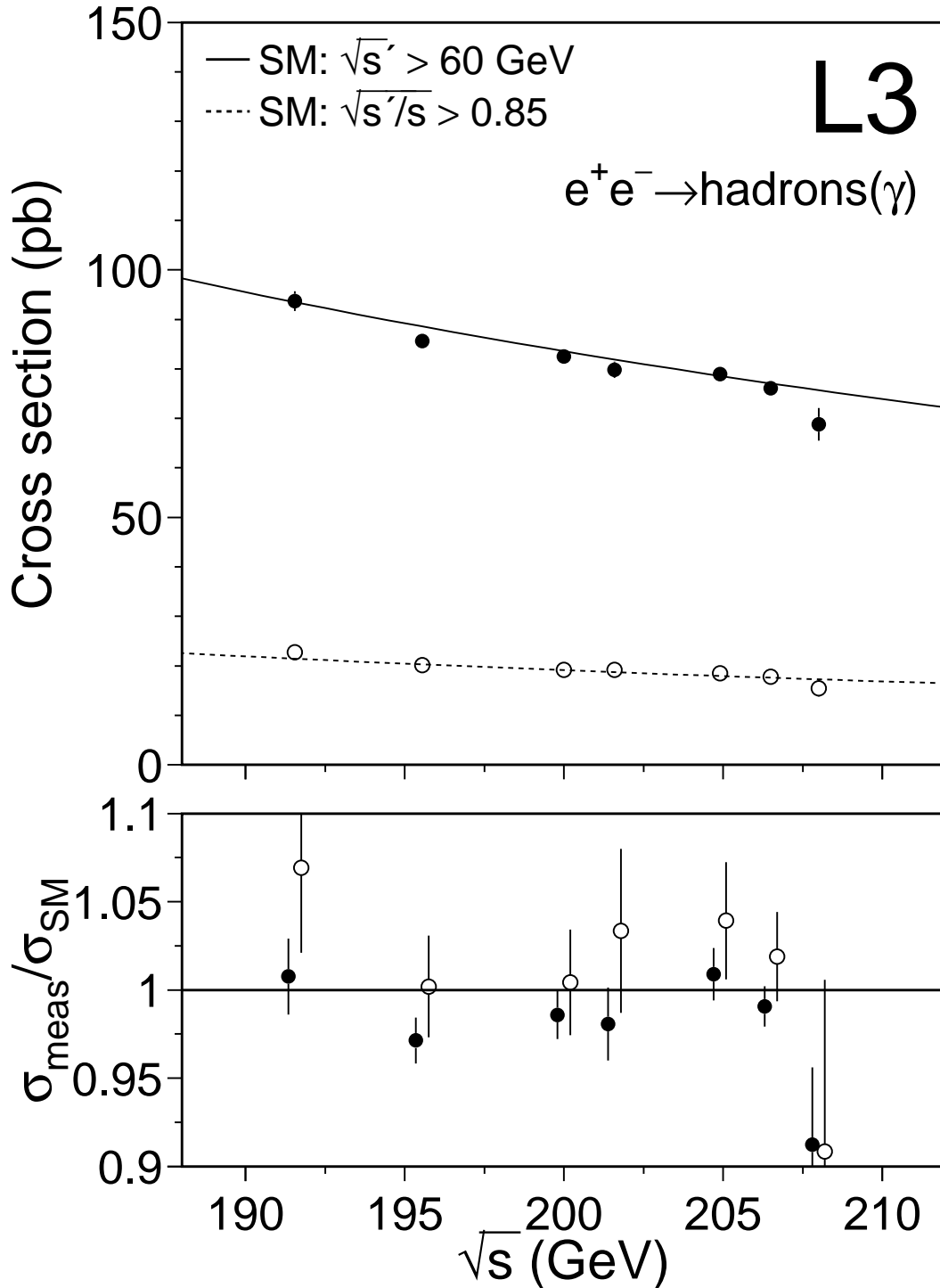
Figure 3: Cross sections of the process $e^+e^- \rightarrow$ hadrons (γ) for the inclusive sample, solid symbols, and the high-energy sample, open symbols. The Standard Model predictions are shown as a solid line for the inclusive sample and as a dashed line for the high-energy sample. The lower plot shows the ratio of measured and predicted cross sections; for clarity, symbols denoting the two final states are slightly shifted. The bars correspond to the sum in quadrature of statistical and systematic uncertainties.
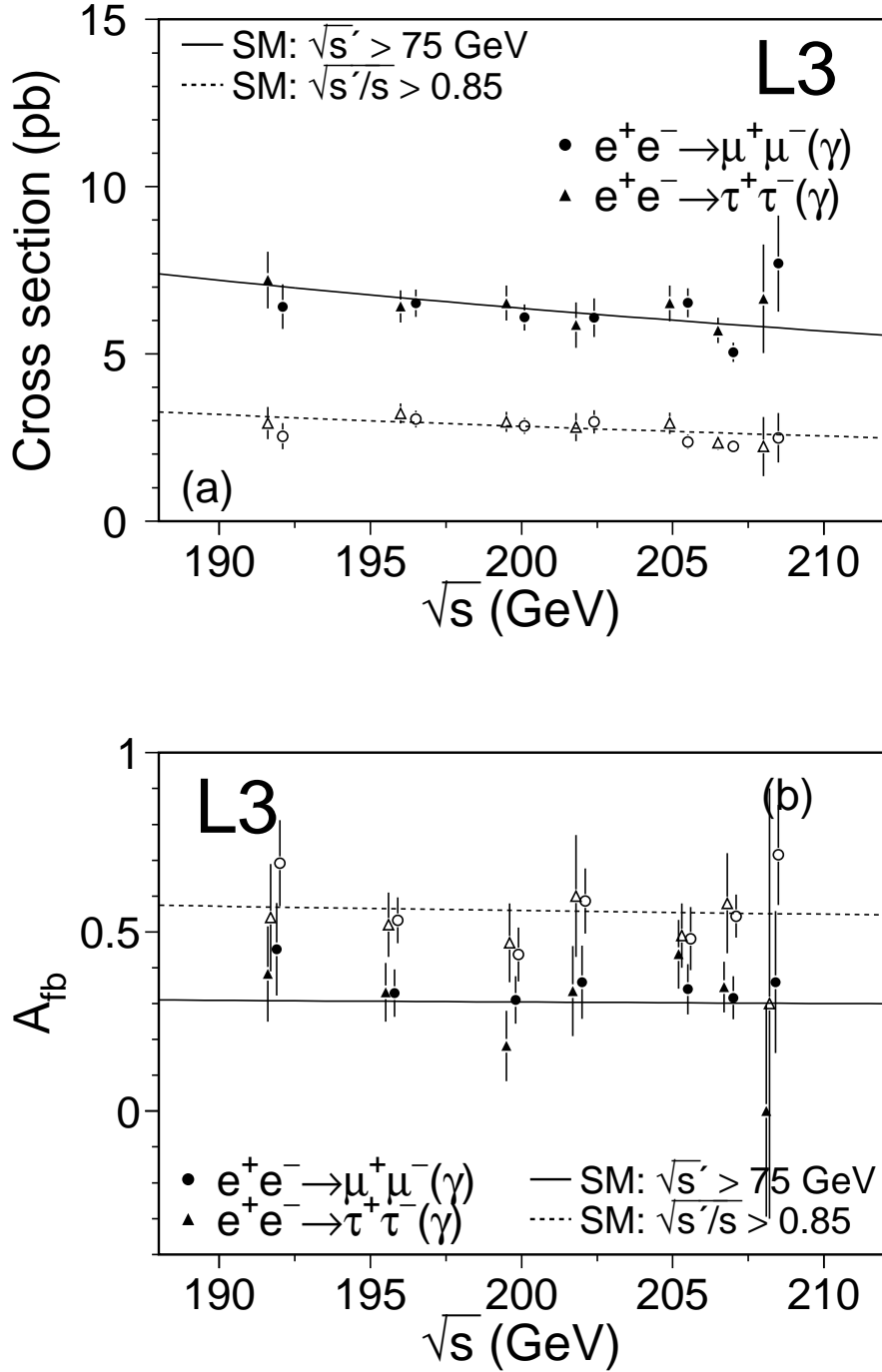
Figure 4: a) Cross sections and b) forward-backward asymmetries, A_{fb}, of the $\mathrm{e^+e^-} \to \mu^+\mu^-(\gamma)$ and $\mathrm{e^+e^-} \to \tau^+\tau^-(\gamma)$ processes for the inclusive sample, solid symbols, and the high-energy sample, open symbols. The Standard Model predictions are shown as solid lines for the inclusive sample and as dashed lines for the high-energy sample. For clarity, the solid and open symbols are slightly shifted. The bars correspond to the sum in quadrature of statistical and systematic uncertainties.
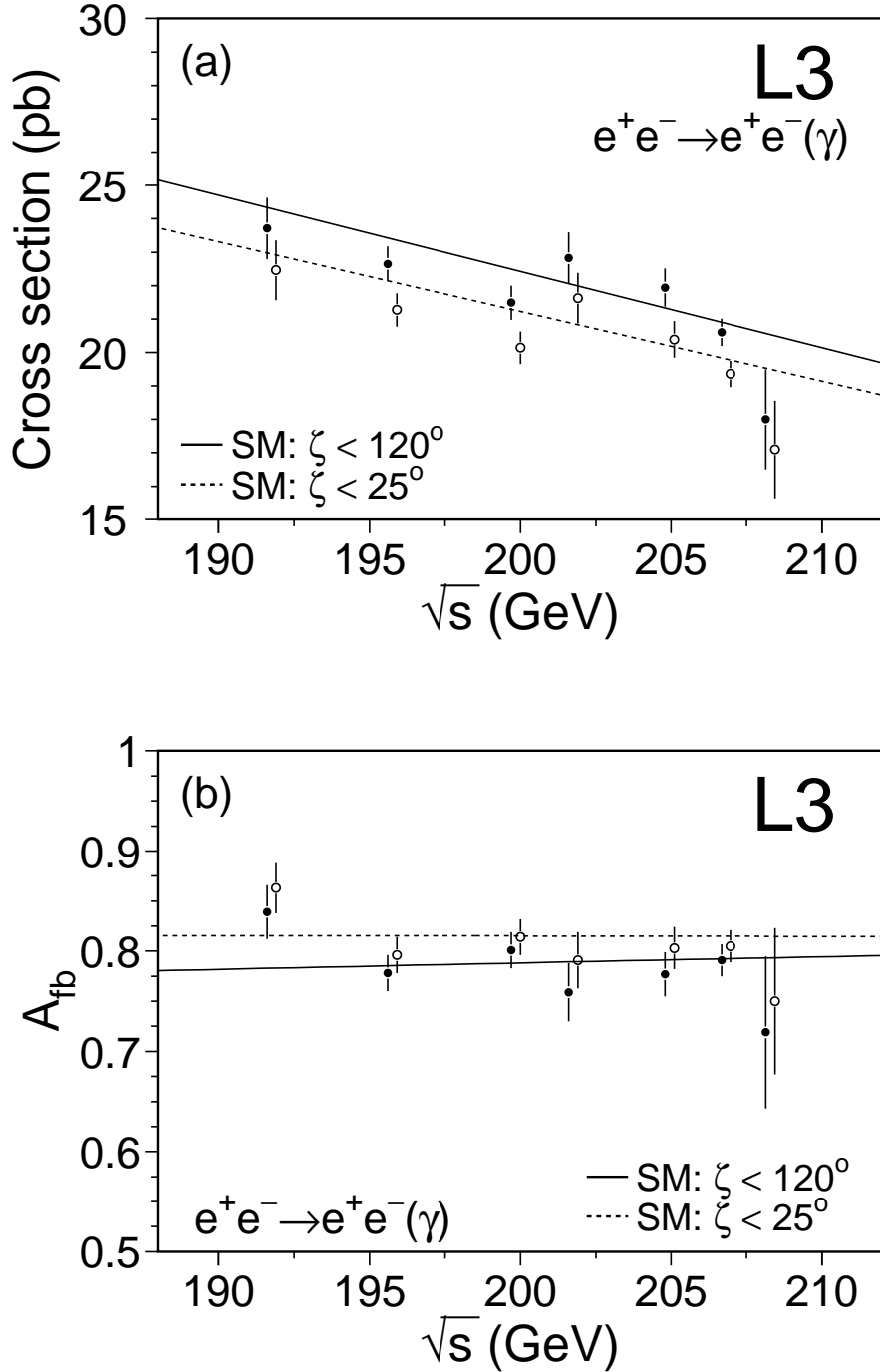
Figure 5: a) Cross sections and b) forward-backward asymmetries, A_{fb}, of the $e^+e^- \to e^+e^-(\gamma)$ process for $|\cos\theta| < 0.72$ for the inclusive sample, solid symbols, and the high-energy sample, open symbols. The Standard Model predictions are shown as solid lines for the inclusive sample and as dashed lines for the high-energy sample. For clarity, the solid and open symbols are slightly shifted. The bars correspond to the sum in quadrature of statistical and systematic uncertainties.
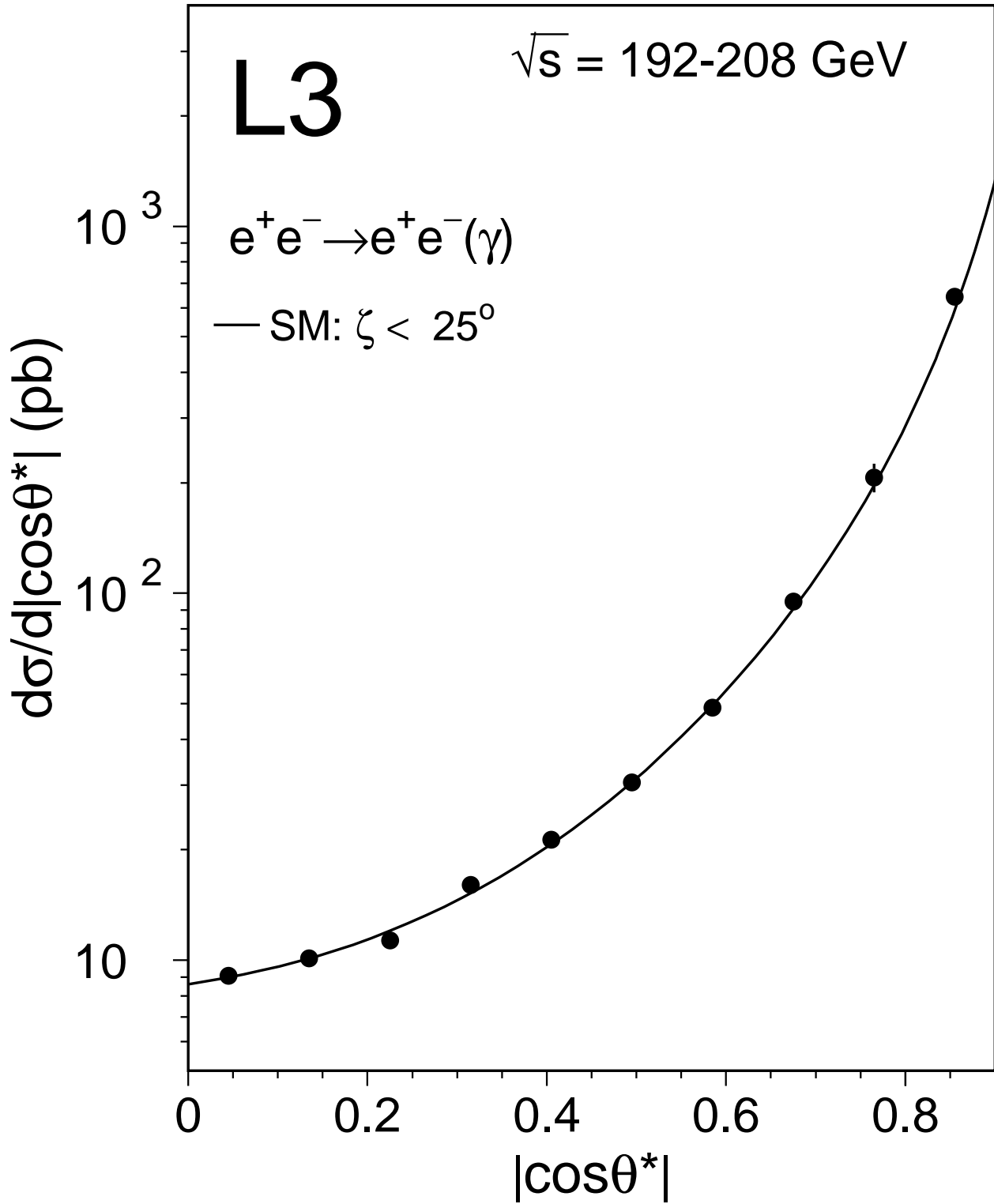
Figure 6: Differential cross section of the $e^+e^- \to e^+e^-(\gamma)$ process for the high-energy sample at $\sqrt{s} = 192-208$ GeV, corresponding to an average centre-of-mass energy $\langle\sqrt{s}\rangle = 201.4$ GeV. The line indicates the Standard Model prediction.
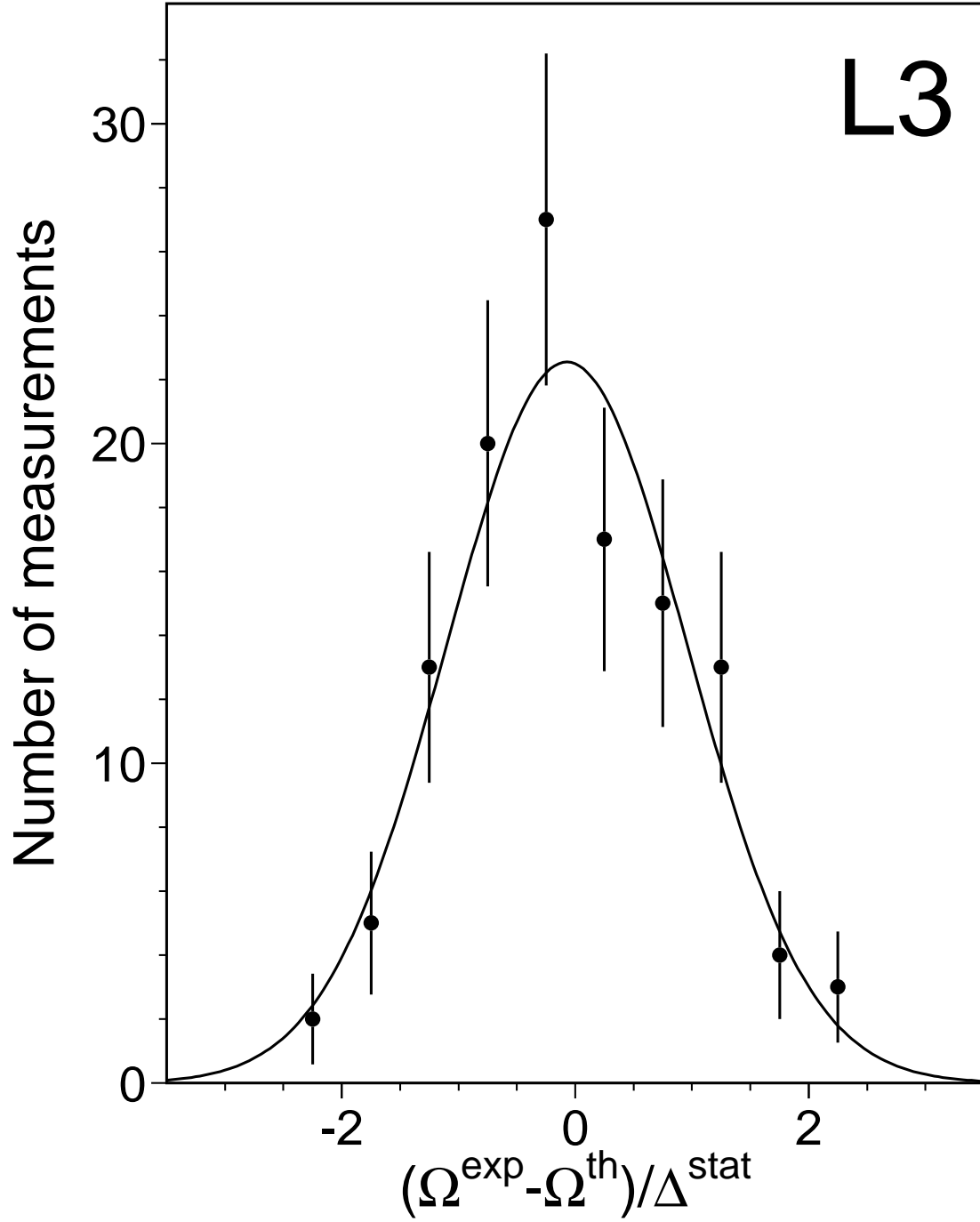
Figure 7: Distribution of the difference of the measured total and differential cross sections and forward-backward asymmetries and the corresponding Standard Model predictions divided by the statistical uncertainty of the measurements. Only the high-energy samples are considered. The line represents the results of a Gaussian fit to this distribution, which finds a mean of -0.07 ± 0.10 and a width of 1.03 ± 0.09, in excellent agreement with the expected spread of the measurements.
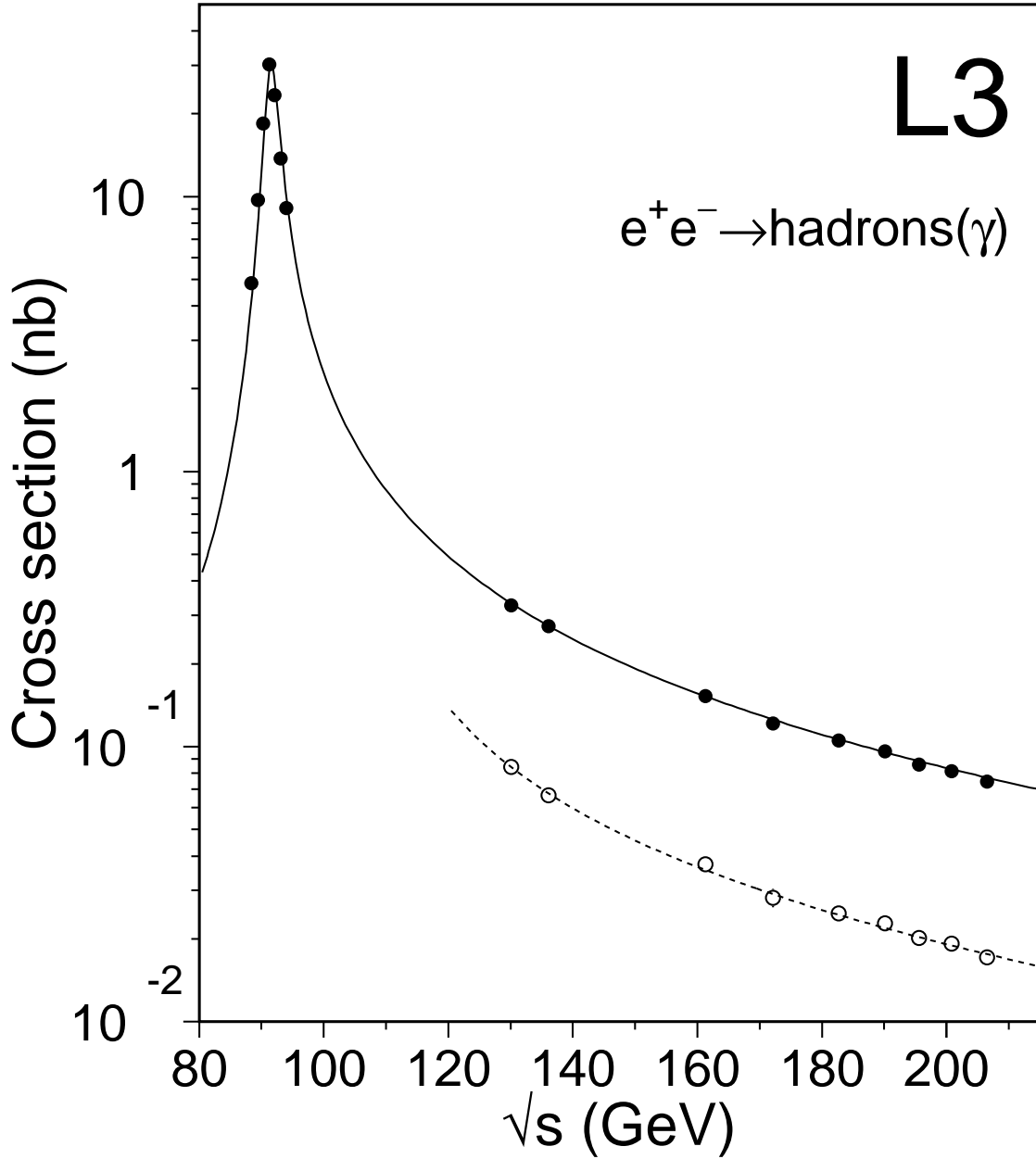
Figure 8: Cross sections of the process $e^+e^- \rightarrow$ hadrons (γ), for the inclusive sample, solid symbols, and the high-energy sample, open symbols. The Standard Model predictions are shown as a solid line for the inclusive sample and as a dashed line for the high-energy sample. The entire LEP data-sample is shown. The bars correspond to the sum in quadrature of statistical and systematic uncertainties.
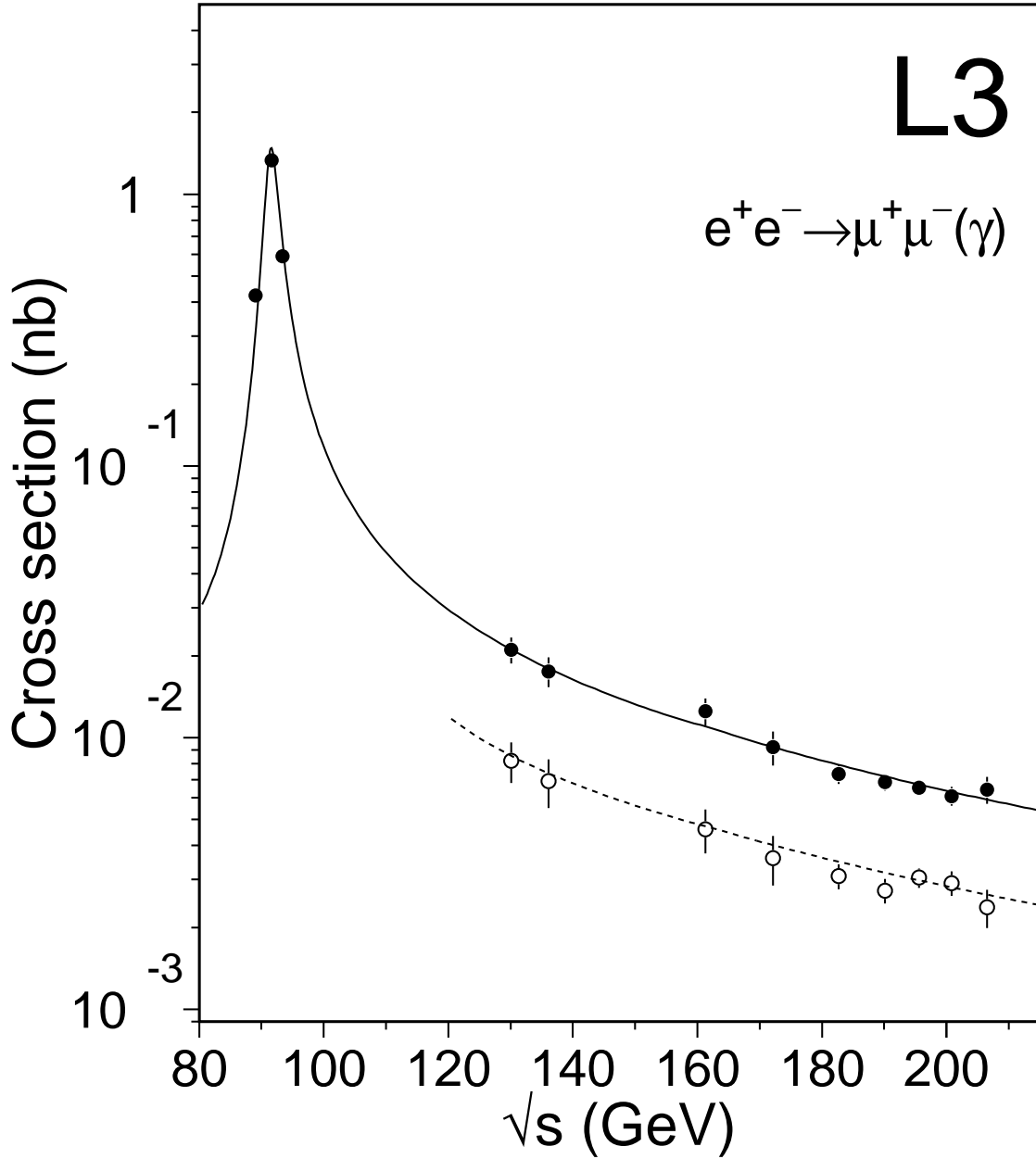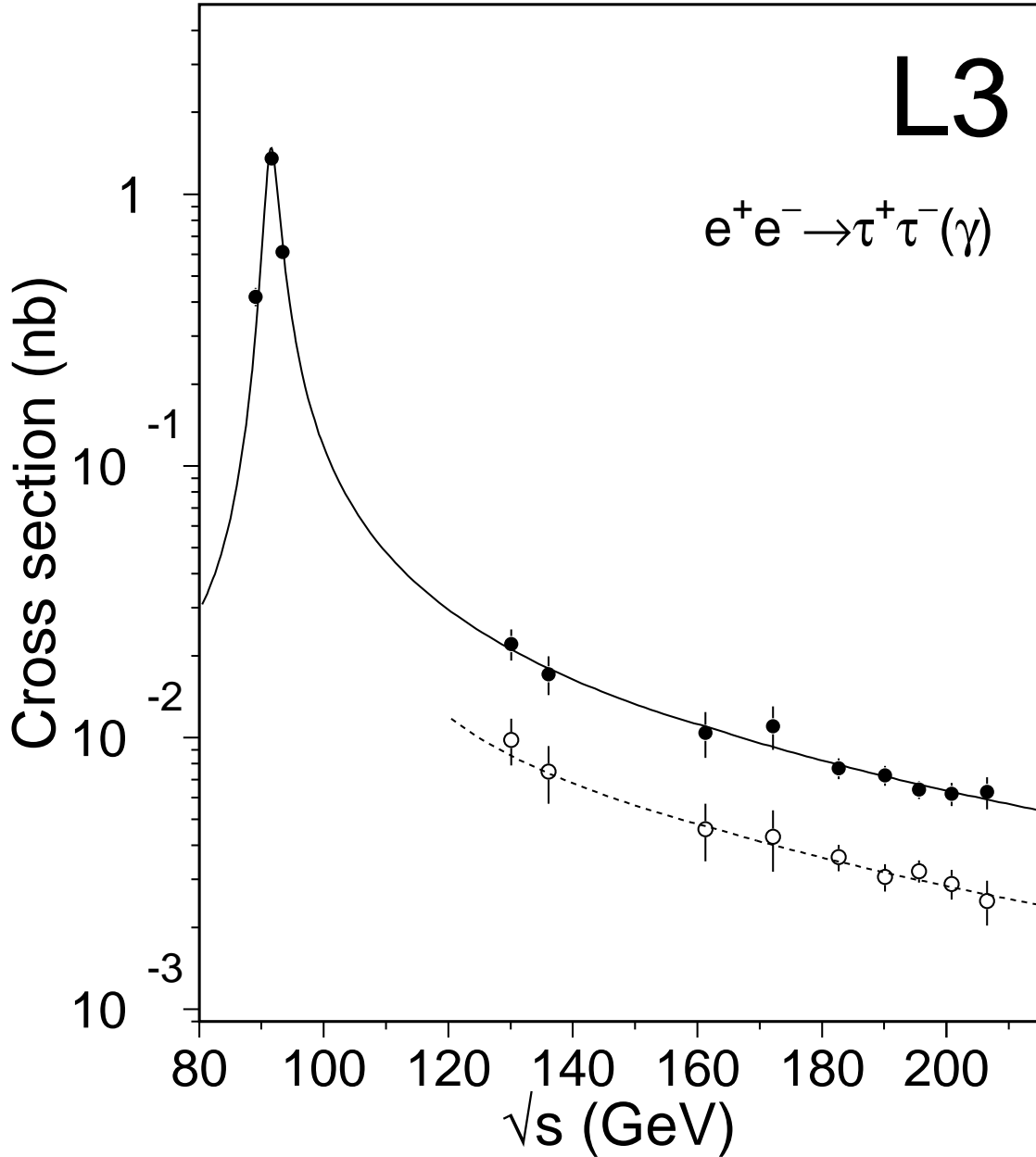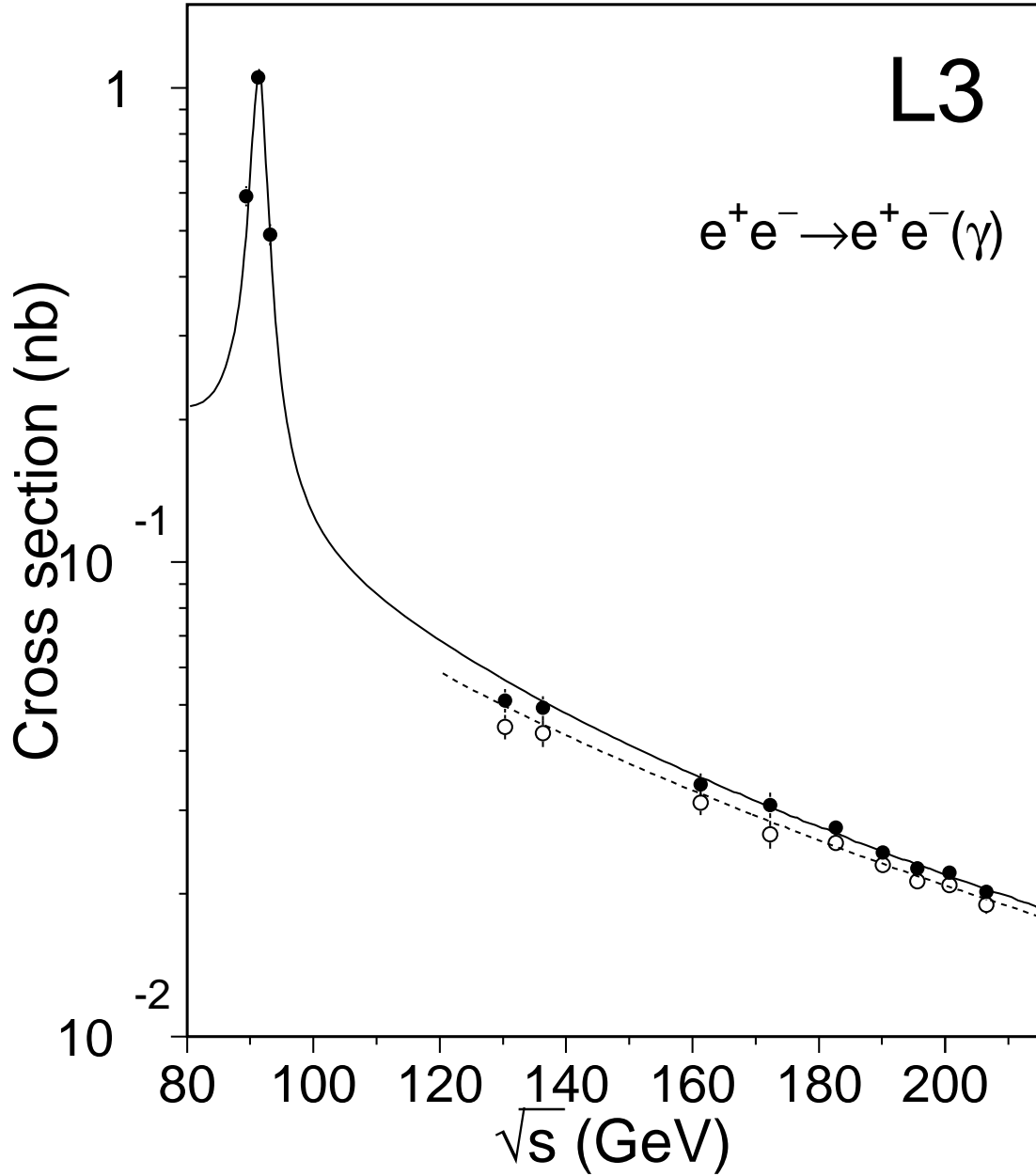
Figure 9: Cross sections of the $e^+e^- \to \mu^+\mu^-(\gamma)$ process for the inclusive sample, solid symbols, and the high-energy sample, open symbols. The Standard Model predictions are shown as solid lines for the inclusive sample and as dashed lines for the high-energy sample. The entire LEP data-sample is shown. The bars correspond to the sum in quadrature of statistical and systematic uncertainties.

Figure 10: Cross sections of the $e^+e^- \to \tau^+\tau^-(\gamma)$ process for the inclusive sample, solid symbols, and the high-energy sample, open symbols. The Standard Model predictions are shown as solid lines for the inclusive sample and as dashed lines for the high-energy sample. The entire LEP data-sample is shown. The bars correspond to the sum in quadrature of statistical and systematic uncertainties.
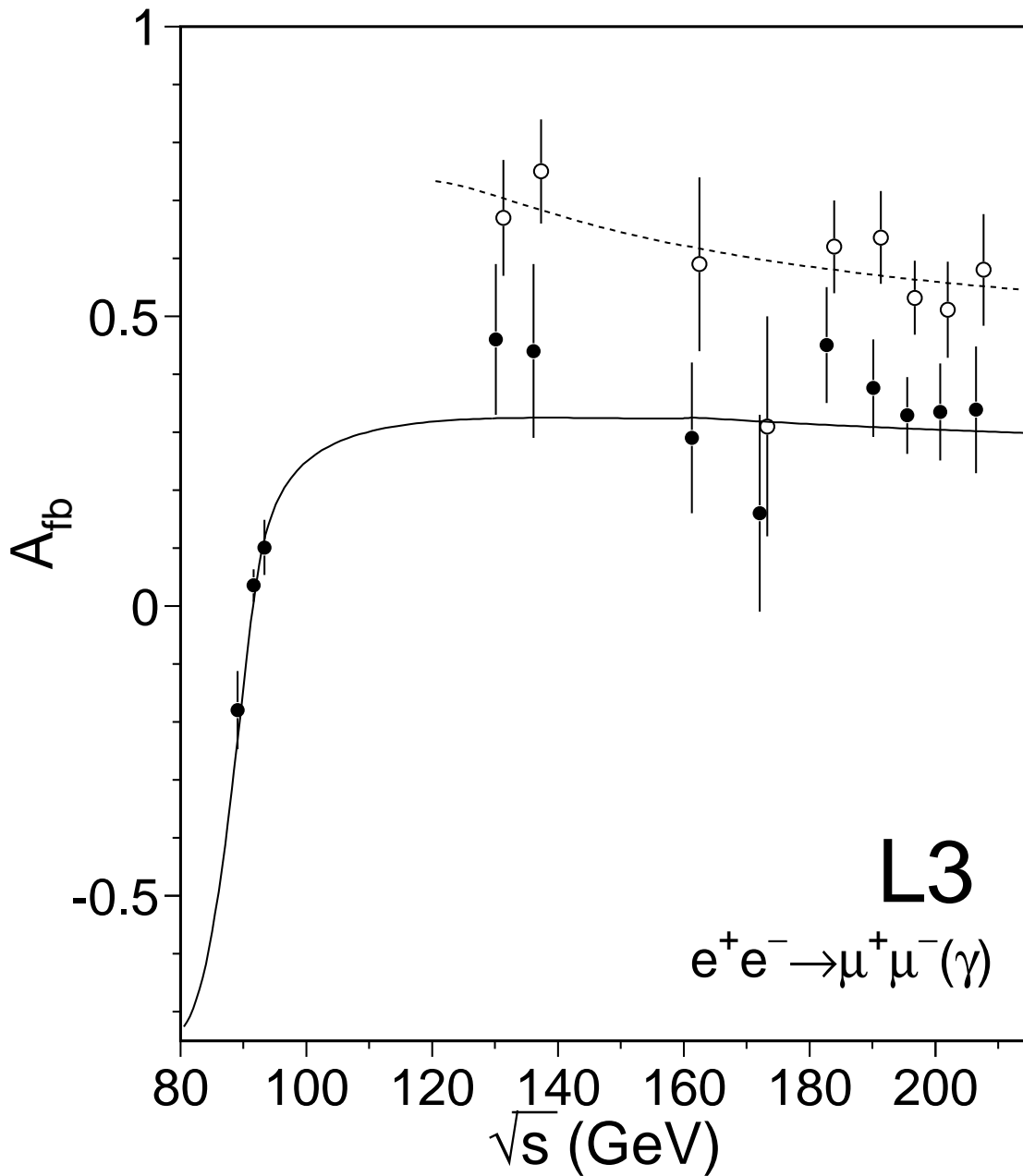
Figure 11: Cross sections of the $e^+e^- \rightarrow e^+e^-(\gamma)$ process in the angular region $|\cos\theta| < 0.72$ for the inclusive sample, solid symbols, and the high-energy sample, open symbols. The Standard Model predictions are shown as solid lines for the inclusive sample and as dashed lines for the high-energy sample. The entire LEP data-sample is shown. The bars correspond to the sum in quadrature of statistical and systematic uncertainties.

Figure 12: Forward-backward asymmetries of the $e^+e^- \rightarrow \mu^+\mu^-(\gamma)$ process for the inclusive sample, solid symbols, and the high-energy sample, open symbols. The Standard Model predictions are shown as solid lines for the inclusive sample and as dashed lines for the high-energy sample. The entire LEP data-sample is shown. For clarity, the solid and open symbols are slightly shifted. The bars correspond to the sum in quadrature of statistical and systematic uncertainties.
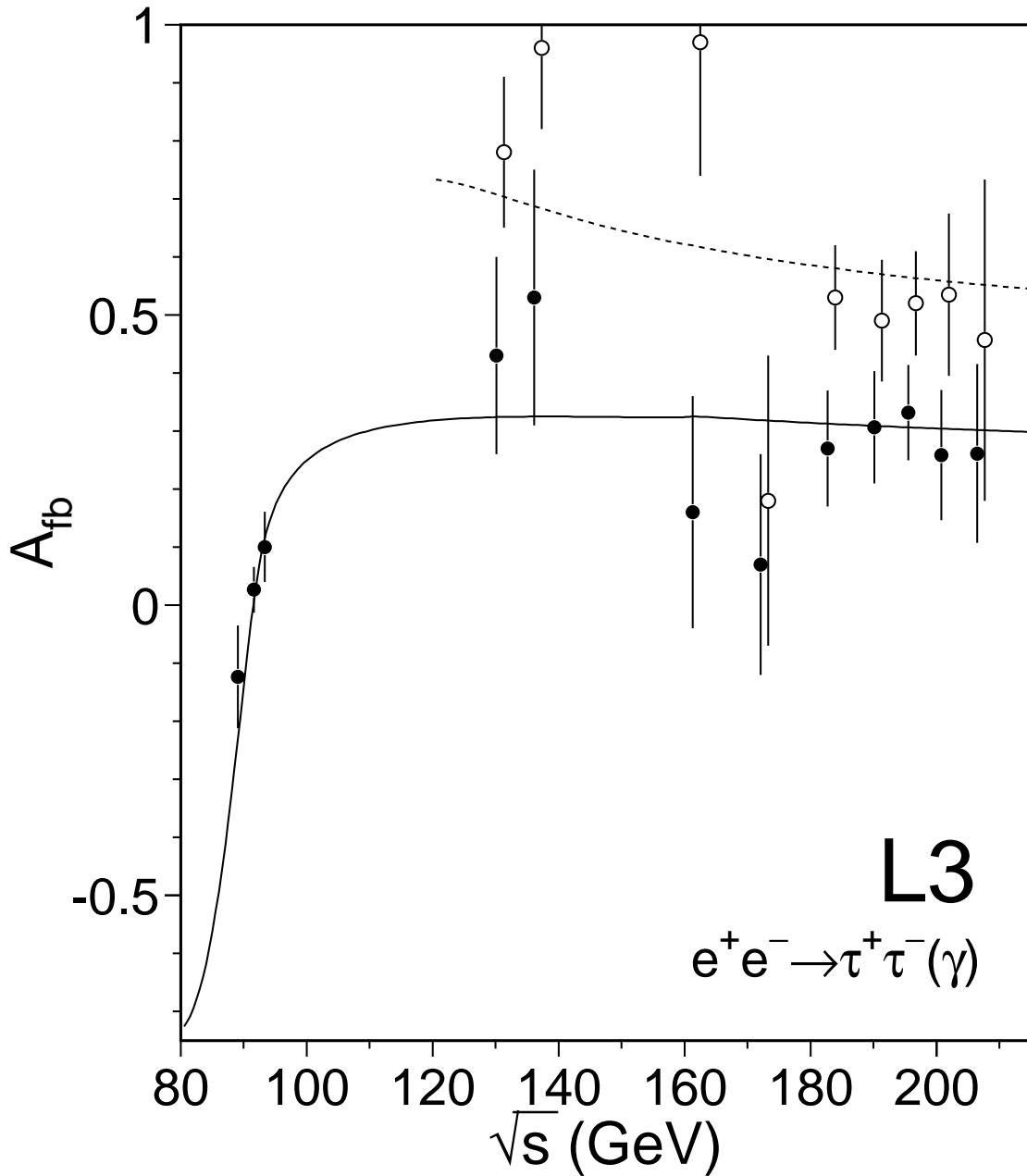
Figure 13: Forward-backward asymmetries of the $e^+e^- \to \tau^+\tau^-(\gamma)$ process for the inclusive sample, solid symbols, and the high-energy sample, open symbols. The Standard Model predictions are shown as solid lines for the inclusive sample and as dashed lines for the high-energy sample. The entire LEP data-sample is shown. For clarity, the solid and open symbols are slightly shifted. The bars correspond to the sum in quadrature of statistical and systematic uncertainties.
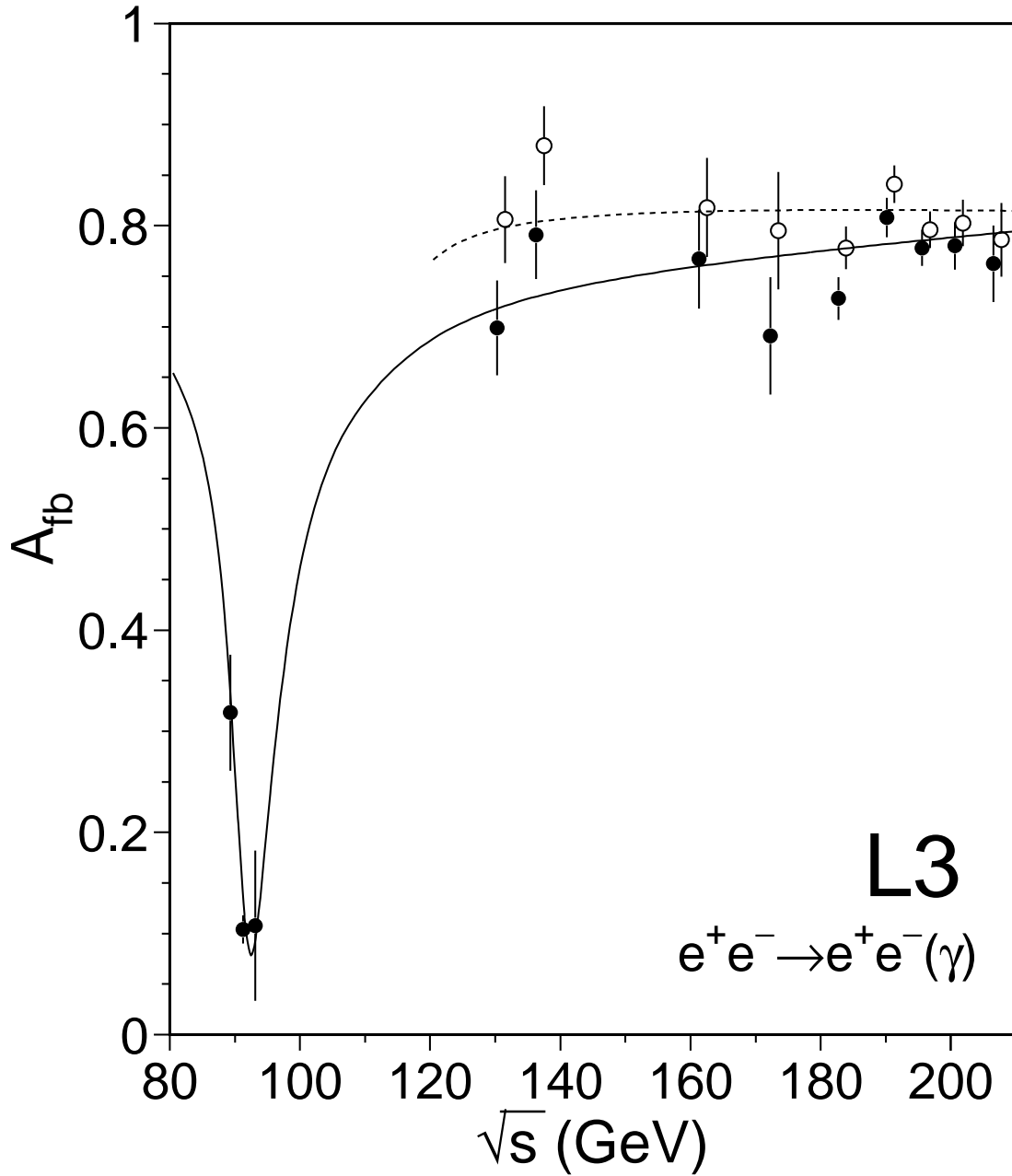
Figure 14: Forward-backward asymmetries of the $e^+e^- \to e^+e^-(\gamma)$ process in the angular region $|\cos\theta| < 0.72$ for the inclusive sample, solid symbols, and the high-energy sample, open symbols. The Standard Model predictions are shown as solid lines for the inclusive sample and as dashed lines for the high-energy sample. The entire LEP data-sample is shown. For clarity, the solid and open symbols are slightly shifted. The bars correspond to the sum in quadrature of statistical and systematic uncertainties.